NTNU – Trondheim
Norwegian University of
Science and Technology

Geomechanical modelling of subsidence and induced seismicity in a gas reservoir

Kyrre Heldal Kartveit

Petroleum Geoscience and Engineering
Submission date: August 2015
Supervisor: Rune Martin Holt, IPT
Co-supervisor: Alexandre Lavrov, SINTEF

Norwegian University of Science and Technology
Department of Petroleum Engineering and Applied Geophysics

Abstract

Reservoir compaction and associated surface subsidence, fault reactivation and induced earthquakes are observed in many petroleum fields worldwide. A better understanding of the geomechanical behaviour of reservoir rocks and neighbouring rock bodies is therefore becoming increasingly important within the petroleum industry. Several monitoring techniques for these phenomena exist, but methods of modelling reservoir geomechanical behaviour are hindered by clear limitations. This study discusses different suspected mechanisms of induced seismicity related to oil and gas production and their significance in varying reservoir environments. In support of this discussion, relevant background theory is presented together with a case study of induced seismicity in the Groningen Gas Field in the northern Netherlands.

The aim of this thesis is to use a Modified Discrete Element Method proposed by (H. T. Alassi, 2008) to model the geomechanical behaviour in a depleting gas reservoir. Multiple scenarios have been modelled to investigate the significance of the suspected underlying mechanisms of seismicity and subsidence observed in the Groningen Field. It was found that depletion of a reservoir has the potential to induce rock failure on faults inside and in contact with the depleted zone as well as causing significant surface subsidence. It is also emphasized that improvements of the method and further research is needed to fully understand the significance of the underlying mechanisms.

Sammendrag

Reservoarkompaksjon og assosiert subsidens, reaktivering av forkastninger og induserte jordskjelv er observert i mange olje- og gassfelt verden over, og økt forståelse av den geomekaniske oppførselen til reservoarbergarter og omkringliggende bergmasse blir stadig viktigere i petroleumsindustrien. Det finnes flere metoder for å monitorere disse fenomenene, men geomekaniske modelleringsmetoder har hittil vært preget av klare begrensninger. Denne studien vil diskutere ulike foreslåtte mekanismer for indusert seismisitet knyttet til olje- og gassproduksjon og deres betydning i ulike reservoarsettinger. Relevant bakgrunnsteori vil bli presentert sammen med et grundig case-studie av indusert seismisitet i Groningen-feltet lokalisert nord-øst i Nederland.

En Modifisert Diskret Elementmetode, foreslått av (H. T. Alassi, 2008), vil bli benyttet til å modellere depletering av et gassreservar og resulterende geomekanisk oppførsel. En rekke modelleringer har blitt utført for å undersøke betydningen av de mulige underliggende mekanismene for den observerte seismisiteten i Groningen-feltet. Studien viser at depletering av et reservoar kan forårsake brudd i forkastninger i og i tilknytning til den depleterte sonen og kan medføre betydelig subsidens. Det er også vektlagt at forbedringer av metoden og videre forskning er nødvendig for å oppnå en fullstendig forståelse av betydningen av de underliggende mekanismene.

Preface

This thesis is carried out as a Master's Thesis in Applied Petroleum Geophysics (TPG4930) at the Norwegian University of Science and Technology (NTNU). The thesis is written at the Department of Petroleum Engineering and Applied Geophysics at NTNU and at SINTEF Petroleum Research, under supervision of Professor Rune Martin Holt and with Senior Scientist Alexandre Lavrov as co-supervisor. The MDEM code used in this thesis is provided by SINTEF. The thesis is written as the final part of my Master's Degree in Petroleum Geosciences.

Trondheim, August 5th

Kyrre Heldal Kartveit

Acknowledgement

First and foremost I give my sincere thanks to my supervisor at the Department of Petroleum Engineering and Applied Geophysics (IPT), Professor Rune Martin Holt. He has given me great guidance and advice throughout my studies at NTNU, and especially during the work on this thesis. He gave me the opportunity to explore my combined interest in geophysics and rock mechanics in an exciting area of study, has expressed enthusiasm and interest for the thesis and been present when needed. Further, I would like to give my acknowledgements to my co-supervisor Alexandre Lavrov and Senior Project Manager at SINTEF, Idar Larsen, for their help with the MDEM code. They are both rock stars in my book, and it is hard to visualize what this thesis had been without their patient guidance. I am grateful to SINTEF for providing me with an office the past year. I also give thanks to Sohrab Gheibi for meaningful discussions during the work on this thesis.

Furthermore I would like to thank students and staff at the department for five brilliant years at NTNU and the IGD group for allowing me to continue my studies at IPT as a PhD fellow.

A wholeheartedly and special thanks to my Mom and Dad.

Table of contents

1 Introduction

Seismic activity in the vicinity of producing hydrocarbon fields has over the last few decades revealed a clear relationship between various human activities and earthquakes. Induced seismicity ranges in magnitudes from undetectable microseismic events to large earthquakes with the potential to cause significant damage to property and population. Only a fraction of the exploited hydrocarbon fields in the world are known to exhibit significant seismicity, however the phenomenon has resulted in a growing socio-economic concern in many regions. On-going research related to unconventional hydrocarbon extraction, geothermal energy projects and geologic storage of gas contributes to our knowledge about reservoir-induced earthquakes.

Underlying mechanisms to the observed seismicity are not yet fully understood. Induced seismicity can result from a number of factors including but not limited to: mining, groundwater extraction, construction of water reservoirs and extraction of fossil fuels. These activities contribute to seismic activity by altering the stresses and strains on the Earth's crust. The most disastrous induced earthquakes historically recorded are probably the events from Kremasta in Greece (1966) and the Koyna Dam in India (1967). Both events where related to reservoir impoundment, with magntitudes of more than 6, causing deaths, injuries and extensive property damage (Suckale, 2009). Induced seismicity associated with hydrocarbon reservoirs are usually much smaller than these events, although several strong earthquake events in Coalinga, USA (1983-1987) and Gazli, Uzbekistan (1976-1984), for example, have been attributed to hydrocarbon production (J.-R. Grasso, 1992). In fields with induced seismicity due to hydrocarbon production, a striking correlation between the observed seismicity and surface subsidence can often be seen. In some cases the subsidence itself is a cause of concern, generally in densely populated areas and in areas close to or below sea level.

The main focus of this thesis is to understand and evaluate the underlying causes of induced seismicity with consideration on producing fault compartmentalized reservoirs, as is the case of the prolific Groningen Field in the Netherlands. Chapters 2 and 3 discuss the theoretical background related to subsidence and induced seismicity, which also encompasses earlier research, observations, and applicable examples. Chapter 4 gives an introduction to earthquake theory focused toward induced seismic activity while Chapter 5 addresses earthquake prediction. A relevant case study of subsidence and seismicity from the Groningen

Field is presented in Chapter 6, complimented by a geomechanical model applicable to the field in Chapter 7. Results from the model are given in Chapter 8 followed by a discussion of the results in Chapter 9. Chapter 10 concludes the thesis.

2 Subsidence

Surface subsidence is a well-documented phenomenon within rock mechanics and can occur due to a number of reasons. Compaction of sediments, fault movement, dissolution of minerals, removal of subsurface fluids and underground mining are all processes or activities that may generate subsidence. In the petroleum industry, challenges related to subsidence and reservoir compaction are well known. Seafloor subsidence associated with the Ekofisk Field (Figure 2.1) reduced the air gap between the offshore platform and sea level, resulting in a jacking operation of the platforms in 1987. Reservoir compaction and subsidence can cause wellbore-casing deformation and significant pipeline damage due to excess compressional or tensional strain (Nagel, 2001). Other risks closely linked with compaction and subsidence include severe flooding, induced earthquakes and weakening of buildings. However, reservoir compaction is not exclusively an undesired phenomenon, for example, it can be a potentially strong production-drive mechanism.

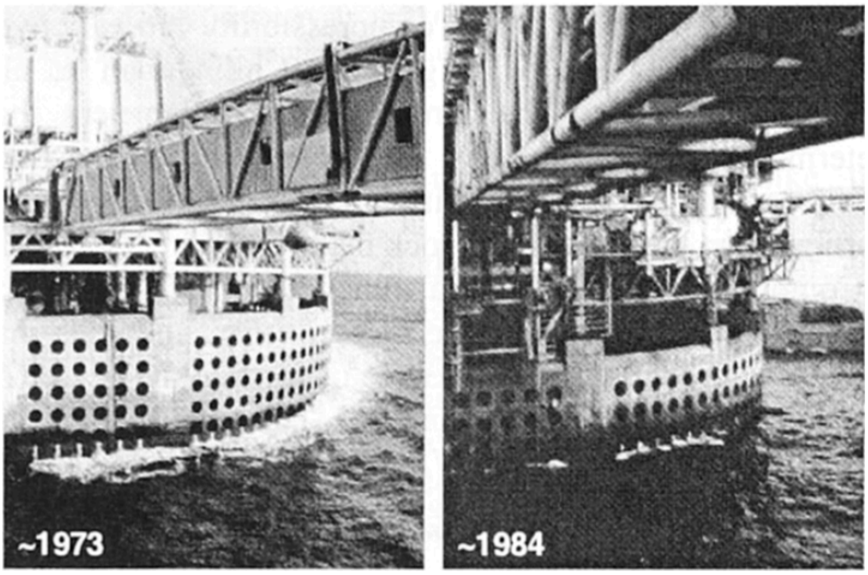

Figure 2.1: Photographs of the 2/4T platform at the Ekofisk field. Subsidence is easily seen by the reduced air gap. Copyright (Nagel, 2001 Figure 5)

2.1 Compaction and Subsidence

A drop in pore pressure due to depletion can cause reservoir compaction, as this will increase the effective stresses in the subsurface. The pressure drop will need to be extensive, but this alone is usually not enough to induce a significant amount of surface subsidence. Compressibility of the reservoir rock and the boundary conditions are important factors, as soft rocks are more likely to compact. In order for subsidence to occur the compaction needs to be significant, meaning that the thickness of the reservoir rock also is of importance. The entire depleted reservoir zone will contribute to compaction, therefore potential adjacent aquifers and overburden must also be evaluated. The overburden may shield the reservoir and prevent subsidence, depending on its geometry, depth, and the contrast in mechanical properties between the reservoir and surrounding rocks (Fjær, Holt, Raaen, Risnes, & Horsrud, 2008).

Not many fields fulfil one or more of these requirements thus considerable subsidence is relatively rare, but because of the potentially severe consequences of subsidence, it is important to evaluate the probability of occurring in advance. The most famous examples of production-induced subsidence may be the Ekofisk and Wilmington oil fields due to the cost of remediation and the amount of subsidence (Mayuga & Allen, 1969; Nagel, 2001), but several other fields throughout the world have experienced similar challenges related to extensive subsidence.

2.1.1 Monitoring of Compaction and Subsidence

Subsidence has traditionally been monitored onshore by levelling and distance surveys. A network of benchmarks is installed around the survey area, where marks outside the subsidence bowl provide fixed reference points. On a regular basis surveys are conducted and the movement of individual stations are analysed, usually using laser techniques. This method provides good accuracy of relative movement, but for larger fields surveys are both time-consuming and prohibitively costly (Nagel, 2001). Although this technique is still commonly used today, its application for offshore fields is restricted and modern systems have phased out the use of levelling surveys within the petroleum sector. Global Positioning System (GPS) stations have been employed to monitor subsidence both onshore and offshore since the 1980's, and the technology has proven to be an accurate and powerful monitoring tool. Under ideal conditions, GPS techniques can detect millimetre-scale elevation changes and are much more cost-effective than traditional levelling surveys. Another important advantage of a GPS system is the possibility to measure subsidence continuously (Mes & Landau, 1995). In offshore applications, GPS monitoring is often combined with bathymetry surveys that measure the local water depth using an echo sounder.

A relatively new addition to the subsidence monitoring portfolio is the Interferometric Synthetic Aperture Radar (InSAR) method. This is a radar technique that utilizes the differences in the phase of electromagnetic radio waves in two or more SAR images to generate a surface deformation map (Landrø, 2010). The SAR imaging system uses microwaves, and thus has cloud penetrating capabilities, and the method is able to measure subsidence with millimeter precision. However, the waves have a poor penetration capability in solids and fluids, and the measurements are often restricted to onshore applications and susceptible to apparent changes in surface elevation due to vegetation.

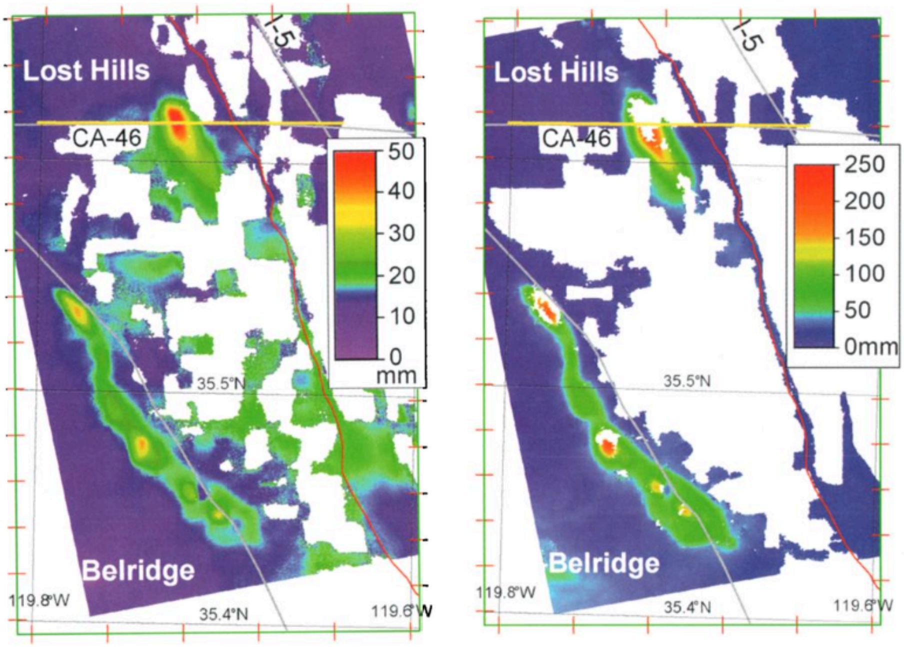

Figure 2.2: Measured subsidence in the San Joaquin Valley, California, converted from satellite SAR data ascending 35 days (left) and 8 months (right). White areas are regions where the phase could not be correlated due to vegetation growth and agricultural activity. Copyright (Fielding, Blom, & Goldstein, 1998 Figures 1 and 2)

Compaction monitoring is essential in order to relate subsidence directly to changes in the subsurface, but is generally a lot more difficult to measure than subsidence. The most commonly used method of measuring reservoir compaction is the use of radioactive markers. Long-lived radioactive sources, usually consisting of Cesium (Cs-137), are placed in a formation at known intervals by a special perforating gun, and can be detected by a number of wireline compaction monitoring tools (Doornhof et al. 2006). Through statistical analysis of the recorded data, the relative displacement of the markers can be estimated with centimetre-scale accuracy. By periodically measuring the distance between the markers, the amount of compaction, and the compaction coefficient of the rock mass, can be measured *in situ*. This technology is best suited for near-vertical wells, as deviated wells introduce error depending on the orientation of the perforation gun when the markers are fired. Care should also be taken into consideration when firing the markers, because if too little charge is used, they may not penetrate the formation properly or they may be knocked loose when the casing is set. If the charge is too large, the markers may be set too far into the formation and the radioactive signature may not be measurable.

The use of time lapse (4D) seismic data is a more recent method of estimating reservoir compaction. These 4D methods are robust, but are still considered to be too imprecise in complex reservoirs e.g. due to sensitivity to shallow gas, fluid substitutions, and non-repeatability. However, the principle that compaction of the reservoir and stretching of the overburden will adjust the velocity profile of the subsurface is adequate to observe time shifts on repeated surveys. Røste et al. and Hatchell et al. proposed in 2005 a method to tie the relative velocity change (*dv/v*) to the relative thickness change (*dz/z*) by introducing a factor R, where:

$$R = -\frac{\frac{dv}{v}}{\frac{dz}{z}} \tag{2.1}$$

Holt et al. (2008) showed through laboratory measurements that this R-factor strongly depends on the stress state and stress path in the subsurface, and that it typically decreases with increasing axial stress (Bjørlykke, 2010). (Røste, Stovas, & Landrø, 2006) establish a simple empirical relationship between velocity and porosity (ϕ):

$$v = a\phi + b \tag{2.2}$$

where *a* and *b* are constants. If we assume that the lateral extent of the reservoir is much larger than its thickness, a simplification can be made by neglecting the lateral strain, and thus only vertical displacement will occur. We refer to this as uniaxial compaction (or stretching). It is now straightforward to show from geometrical considerations that the thickness change is related to porosity change by:

$$\frac{dz}{z} = \frac{d\phi}{1-\phi} \tag{2.3}$$

If we then insert equations (2.2) and (2.3) into equation (2.1) we obtain a new expression for the R-factor:

$$R = 1 - \frac{a+b}{v} \tag{2.4}$$

The relation between an observed time shift and the velocity and thickness changes is given as:

$$\frac{dT}{T} = \frac{dz}{z} - \frac{dv}{v} = (1+R)\frac{dz}{z} = -\left(\frac{1+R}{R}\right)\frac{dv}{v} \tag{2.5}$$

The relative change in thickness can now be estimated by inserting equation (2.4) into equation (2.5):

$$\frac{dz}{z} = \left(\frac{v}{2v-a-b}\right)\frac{dT}{T} = S\frac{dT}{T} \tag{2.6}$$

where S is the strain-timestrain ratio representing how much the relative displacement is for a given measured relative time shift. If the velocity profile and the empirical parameters a and b are known, we can estimate $S(z)$. This is a simplified model and it must be emphasized that stress changes and stress paths are also of great importance when considering volume strains. Various methods that tie seismic changes to geomechanical models are still being developed and improved. This technique has been successfully executed in several fields from the North Sea, including the Ekofisk and Valhall Fields (Bjørlykke, 2010). (See also Section 2.2.2).

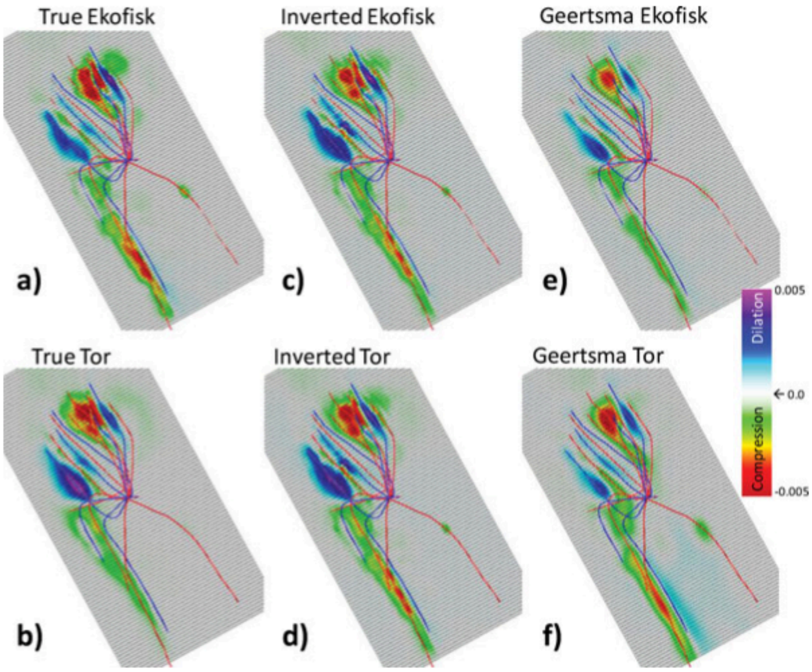

Figure 2.3: (a) and (b) show the computed reservoir volumetric strain for production and injection into the Ekofisk and Tor reservoirs in a survey period between 1995 and 2005. (c) and (d) show the corresponding strains estimated by (Garcia & MacBeth, 2013) using the inversion method described in section 2.2.2, and (e) and (f) are the result of the Green's function approach described by (Geertsma, 1973). Copyright (Garcia & MacBeth, 2013 Figure 10)

Since compaction leads to pore volume loss and microfracture generation, porosity logging and passive seismic monitoring can also be used to detect reservoir compaction. These methods, however, have great limitations in accuracy and provide a more qualitative indication of compaction than the techniques previously described.

2.1.2 Modelling of Compaction and Subsidence

Due to the potentially large impact of compaction and subsidence, many models for predicting and modelling of reservoir compaction and associated subsidence have been proposed over the past decades. For a thorough description of these models the reader is referred to (Fjær et al., 2008; Geertsma, 1966; Segall, 1992). However, a short review of the basic background principles will be given from (Fjær et al. 2008).

If we consider a homogeneous reservoir consisting of isotopic rock and assume linear poroelasticity, deformation in the reservoir can be expressed by Hooke's law in terms of change in effective Earth stresses:

$$E_{\mathrm{fr}}\varepsilon_{\mathrm{h}} = \Delta\sigma'_{\mathrm{h}} - \nu_{\mathrm{fr}}(\Delta\sigma'_{\mathrm{H}} + \Delta\sigma'_{\mathrm{v}}) \qquad (2.7)$$

$$E_{\mathrm{fr}}\varepsilon_{\mathrm{H}} = \Delta\sigma'_{\mathrm{H}} - \nu_{\mathrm{fr}}(\Delta\sigma'_{\mathrm{h}} + \Delta\sigma'_{\mathrm{v}}) \qquad (2.8)$$

$$E_{\mathrm{fr}}\varepsilon_{\mathrm{v}} = \Delta\sigma'_{\mathrm{v}} - \nu_{\mathrm{fr}}(\Delta\sigma'_{\mathrm{H}} + \Delta\sigma'_{\mathrm{h}}) \qquad (2.9)$$

where E_{fr} is the framework Young's modulus, ε is strain, $\nu_{\mathrm{fr}}$is the Poisson's ratio and $\Delta\sigma'$ signify the change in effective stress defined as

$$\Delta\sigma'_{\mathrm{v}} = \Delta\sigma_{\mathrm{v}} - \alpha\Delta p_{\mathrm{f}} \qquad (2.10)$$

$$\Delta\sigma'_{\mathrm{H}} = \Delta\sigma_{\mathrm{H}} - \alpha\Delta p_{\mathrm{f}} \qquad (2.11)$$

$$\Delta\sigma'_{\mathrm{h}} = \Delta\sigma_{\mathrm{H}} - \alpha\Delta p_{\mathrm{f}} \qquad (2.12)$$

where α is the Biot coefficient. We then assume uniaxial compaction:

$$\varepsilon_{\mathrm{h}} = \varepsilon_{\mathrm{H}} = 0 \qquad (2.13)$$

To keep the uniaxial condition during depletion, the effective horizontal stresses have to increase. By inserting equation (2.13) into equations (2.7-2.8) we find:

$$\Delta\sigma'_{\mathrm{h}} = \Delta\sigma'_{\mathrm{H}} = \frac{\nu_{\mathrm{fr}}}{1-\nu_{\mathrm{fr}}}\Delta\sigma'_{\mathrm{v}} \qquad (2.14)$$

We also assume that the total vertical stress acting on the rock mass remains constant during depletion ($\Delta\sigma_{\mathrm{v}} = 0$), and thus neglect the effect of stress arching:

$$\Delta\sigma_{\mathrm{v}}' = \Delta\sigma_{\mathrm{v}} - \alpha\Delta p_{\mathrm{f}} = -\alpha\Delta p_{\mathrm{f}} \tag{2.15}$$

The change in the reservoir thickness Δh can be given by the vertical strain ε_{v} and the reservoir thickness h,

$$\Delta \mathrm{h} = -\varepsilon_{\mathrm{v}} \mathrm{h} \tag{2.16}$$

or by the compaction coefficient Cm, the poroelastic coefficient α, the change in pore pressure and the thickness:

$$\frac{\Delta \mathrm{h}}{\mathrm{h}} = C_{\mathrm{m}}\alpha\Delta p_{\mathrm{f}} \tag{2.17}$$

The compaction coefficient, also known as uniaxial compressibility, is a function of a number of parameters, including the minerals that make up the rock mass, degree of sorting, cementation and porosity. Porosity is often considered the critical indicator of the compressibility but it is still very difficult to accurately measure, particularly on a rock mass scale. Furthermore, the uniaxial compressibility is equal to the inverse of the framework uniaxial compaction modulus:

$$C_{\mathrm{m}} = \frac{1}{E_{\mathrm{fr}}}\frac{(1+\nu_{\mathrm{fr}})(1-2\nu_{\mathrm{fr}})}{1-\nu_{\mathrm{fr}}} = \frac{1}{3K_{\mathrm{fr}}}\frac{1+\nu_{\mathrm{fr}}}{1-\nu_{\mathrm{fr}}} = \frac{1}{H_{\mathrm{fr}}} = \frac{1}{\lambda_{\mathrm{fr}} + 2G_{\mathrm{fr}}} \tag{2.18}$$

This uniaxial compaction modulus corresponds to the plane wave modulus measured in, or corrected to, dry conditions. The dynamic moduli are normally larger than the corresponding static ones, and therefore a direct estimate of compaction from sonic data will most likely provide a minimum estimate of the true compaction. This difference is largest for weak rocks and is reduced with increasing confinement.

We can now estimate the compaction caused by depletion by inserting for all three principal stress changes in equation (2.9), given that the elastic properties (E_{fr} and ν_{fr}), the poroelastic coefficient and the reservoir thickness are known:

$$\frac{\Delta \mathrm{h}}{\mathrm{h}} = \frac{1}{E_{\mathrm{fr}}}\frac{(1+\nu_{\mathrm{fr}})(1-2\nu_{\mathrm{fr}})}{1-\nu_{\mathrm{fr}}}\alpha\Delta p_{\mathrm{f}} \tag{2.19}$$

A main problem with this simple compaction solution is that the mechanical properties and the pressure distribution will not be uniform in a field, and it may be hard to estimate accurate values for the parameters involved. Changes in reservoir pressure will not only induce change in the effective stress, but also in the total stress distribution acting on the reservoir and surrounding rock. Averaging values obtained throughout a study area can give very unreliable results for great parts of the area. The reservoir stress path was defined by (Hettema et al. 2000) in means of the stress path coefficients.

$$\gamma_{\mathrm{v}} = \frac{\Delta\sigma_{\mathrm{v}}}{\Delta p_{\mathrm{f}}} \tag{2.20}$$

$$\gamma_{\mathrm{H}} = \frac{\Delta\sigma_{\mathrm{H}}}{\Delta p_{\mathrm{f}}} \tag{2.21}$$

$$\gamma_{\mathrm{h}} = \frac{\Delta\sigma_{\mathrm{h}}}{\Delta p_{\mathrm{f}}} \tag{2.22}$$

As mentioned earlier, in our uniaxial example the arching coefficient, γ_{v}, will be zero, while γ_{h}=γ_{H} describe the change in the horizontal stress field.

The stress path coefficients may also be defined in terms of the effective stresses, this gives the relation:

$$\gamma' = \gamma - \alpha \tag{2.23}$$

The ratio between effective horizontal and vertical stress changes, κ, can be defined as another stress path coefficient:

$$\kappa = \frac{\Delta\sigma_{\mathrm{h}}'}{\Delta\sigma_{\mathrm{v}}'} \tag{2.24}$$

By inserting equation (2.10) and (2.12) in (2.24), we obtain

$$\kappa = \frac{1 - \frac{\gamma_{\mathrm{h}}}{\alpha}}{1 - \frac{\gamma_{\mathrm{v}}}{\alpha}} = \frac{\alpha - \gamma_{\mathrm{h}}}{\alpha - y_{\mathrm{v}}} = \frac{\gamma_{\mathrm{h}}'}{\gamma_{\mathrm{v}}'} \tag{2.25}$$

For uniaxial compaction, this coefficient can simply be derived from (2.14):

$$\kappa = \frac{\nu_{\mathrm{fr}}}{1 - \nu_{\mathrm{fr}}} \tag{2.26}$$

Thus by combining (2.25) and (2.26) we get:

$$\gamma_{\mathrm{h}} = \gamma_{\mathrm{H}} = \alpha \frac{1 - 2\nu_{\mathrm{fr}}}{1 - \nu_{\mathrm{fr}}} \tag{2.27}$$

This was the default assumption in the industry for a long time, before the strong influence of the stress path was recognized through analysis of compaction and subsidence in hydrocarbon fields (see e.g. Hettema et al., 2000; Teufel et al. 1991). We can calculate elastic reservoir compaction for a general stress path by combining Hooke's law, equations (2.16), (2.20) and (2.22), which gives us:

$$\frac{\Delta \mathrm{h}}{\mathrm{h}} = \frac{\alpha}{E_{\mathrm{fr}}} \left[\left(1 - \frac{\gamma_{\mathrm{v}}}{\alpha}\right) - 2\nu_{\mathrm{fr}} \left(1 - \frac{\gamma_{\mathrm{h}}}{\alpha}\right) \right] \Delta p_{\mathrm{f}} = -\frac{1}{E_{\mathrm{fr}}} [\gamma_{\mathrm{v}}' - 2\nu_{\mathrm{fr}} \gamma_{\mathrm{h}}'] \Delta p_{\mathrm{f}} \tag{2.28}$$

The stress evolution during depletion depends mainly on the reservoir geometry, the elastic contrast between reservoir and surrounding rock mass and the initial stress state prior to production (Segura et al., 2011). In a soft reservoir surrounded by a stiff bounding material, the stress arching coefficient will be high and the stress will be concentrated as unloading in the overburden and loading in the sideburden, while the depleting zone will be shielded. The horizontal stress path coefficient, γ_{h}, depends on the boundary conditions at the sides of the reservoir (e.g. assuming negligible horizontal strain in the uniaxial case) and is usually estimated in the field by hydraulic fracturing tests (see Section 2.2).

Several models have been proposed to tie surface subsidence to reservoir compaction. Burial depth, reservoir size, and the elastic and poroelastic properties of the reservoir are the dominating factors for the amount of subsidence (Geertsma, 1973; Suckale, 2009). (Segall, Grasso, & Mossop, 1994) computed a poroelastic model to compute the stress and deformation fields induced by gas extraction in the area around the Lacq Field in soutwestern France. Their approach was based on earlier work on stress alteration due to fluid extraction by (Segall, 1989), linear poroelasticity and used a simple Mohr-Coulomb failure criterion.

For an isotropic poroelastic medium, the solid volume strain, $\varepsilon_{\mathrm{kk}}$, can be expressed as:

$$\varepsilon_{\mathrm{kk}} = \frac{\sigma_{\mathrm{kk}}}{3K} + \frac{\alpha p_{\mathrm{f}}}{K} \tag{2.29}$$

Where K is the undrained bulk modulus, α is the Biot pore pressure coefficient, $\sigma/3$ is the mean stress and p_{f} is pore pressure. Einstein notation is used, which implies summation over repeated indices.

If we know or can simulate the pore pressure field, displacements and stresses can be computed, according to (Geertsma, 1966), from a distribution of centers of dilatation with strengths proportional to $\alpha p(x)$. In an axisymmetric situation, production-induced pore pressure changes depend only on radial distance and depth, $p(r,z)$. The displacements are thus given as:

$$u_i(r,z) = \frac{\alpha}{\mu}\int_0^\infty \int_0^\infty p(\rho,d) g_i(r,z;\rho,d) d\rho dd \tag{2.30}$$

where μ is the shear modulus. The Green's functions, $g_i(r,z;\rho,d)$, correspond to a ring of dilatation at radius ρ and depth d.

Given the displacements, the stresses are computed from the strains and the theory of linear poroelasticity:

$$\sigma_{ij}(r,z) = \alpha\frac{(1-2v)}{2(1-v)} \times \int_0^\infty \int_0^\infty \frac{\partial p(\rho,d)}{\partial \rho} G_{ij}(r,z;\rho,d) d\rho dd - p\delta_{ij} \tag{2.31}$$

Where the G_{ij} contributions are related to the displacement Green's functions via (Segall, 1992):

$$G_{ij} = \frac{\partial g_i}{\partial x_j} + \frac{\partial g_j}{\partial x_i} + \frac{2v}{1-2v}\frac{\partial g_k}{\partial x_k}\delta_{ij} \tag{2.32}$$

The maximum displacement at the surface will be given by

$$u_z(0,0) = -\frac{\alpha(1-2v)T\Delta p}{\mu}\left[1 - \frac{\frac{d}{R}}{\sqrt{1+(\frac{d}{R})^2}}\right] \tag{2.33}$$

assuming the reservoir is disk-shaped with radius R, thickness T that is small in comparison to its depth, and uniform pressure decline. This shows a linear relationship between the maximum subsidence and pressure decline, which corresponds very well with the observed data from the Lacq Field (Figure 2.4).

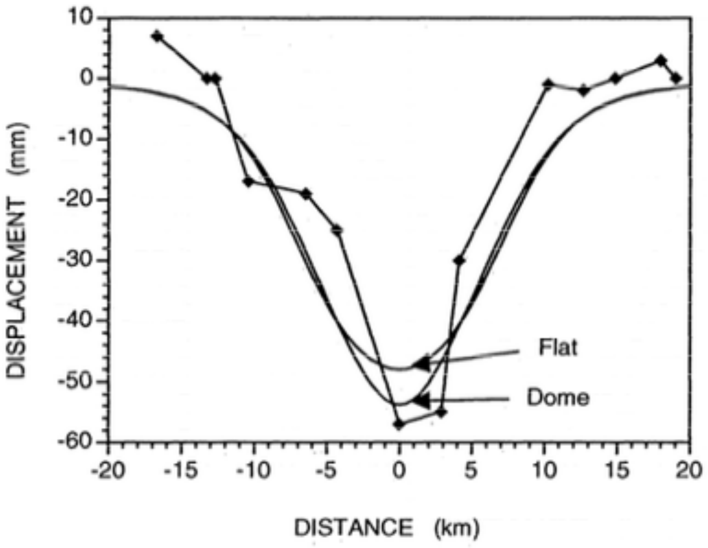

Figure 2.4: Vertical displacement at the Lacq field predicted by (Segall et al., 1994) compared to leveling results for the time interval 1887-1989. Two predicted models are shown, one considering the reservoir as a flat layer and the other including the effect of a dome structure. Copyright (Segall et al., 1994 Figure 9)

2.2 In-situ Stress

As previously discussed, knowledge about the in-situ stress and stress changes in and around a reservoir is of upmost importance in order to understand and predict induced seismicity. The mechanical properties of the subsurface are also closely connected with wellbore stability problems, subsidence, fracturing operations and sand production evaluation (Fjær et al., 2008). There are a limited number of methods to estimate these properties. A brief description of how to use poroelastic theory to connect pressure changes in the reservoir with stress distribution has been given, however it is essential to know the initial stresses in the reservoir prior to poroelastic modelling. Methods for determining in-situ stresses are generally associated with different well logs and -tests or laboratory measurements, but conducting a leak-off test will often give the most accurate prediction of the minimal horizontal stress.

2.2.1 Leak-Off Test and Extended Leak-Off Test

Leak-off tests (LOTs) and extended leak-off tests (ELOTs) are performed during the drilling phase of a well to estimate maximum well pressure and in-situ stress. LOTs have traditionally been used to assess casing integrity and to evaluate mud density for a new borehole section. After setting a casing in a well, a LOT can be executed by drilling through the casing shoe and penetrate a few metres of new formation. Next, the annulus is closed and fluid is pumped into the open hole section at a constant rate, generally 50-250 l/min, allowing no flow out of the well. Pressure versus time will plot as a straight line dependent primarily on the compressibility of the drilling fluid, until the leak-off point is reached where the pressure-rate declines due to fracture generation (Fjær et al., 2008). The LOT is normally stopped shortly after this occurs. The leak-off point is not necessarily directly related to the smallest horizontal stress, and even if the shut-in phase is recorded this may overestimate the sought value. Stress information is derived by using two different approaches, namely the analysis of individual LOTs or empirical correlations of large numbers of data in a basin or field. In a best-case scenario data from a number of LOTs can provide an estimate of the minimum horizontal stress in a formation, however the maximum horizontal stress is rarely addressed. Stress estimations from LOTs are plagued by the fact that there is no standard methodology in the industry, the tests are invariably performed in shales and should not be extrapolated directly to other lithologies, and that the mechanics and interpretation of the test are poorly understood. The need for stress information in exploration and drilling planning has driven the LOT to be developed further and generating the ELOT which has sufficient accuracy and reliability to be used as a stress estimation method (Addis, Hanssen, Yassir, Willoughby, & Enever, 1998).

The ELOT is performed similarly to a LOT, but instead of stopping the pump after the leak-off point is reached, pumping continues well beyond this and also beyond the breakdown pressure. After shut-in, the shut-in phase should be recorded, and usually the test is repeated for two or more pressurisation cycles: This is done in order to overcome the tensile strength and stress concentration around the borehole to obtain a stable fracture growth, and therefore the second and third shut-in pressures are usually better estimates of the minimum stress magnitude than the first one. Each recorded curve must be investigated and related to other available information about drilling and lithology before the data is used for stress evaluation (Addis et al., 1998).

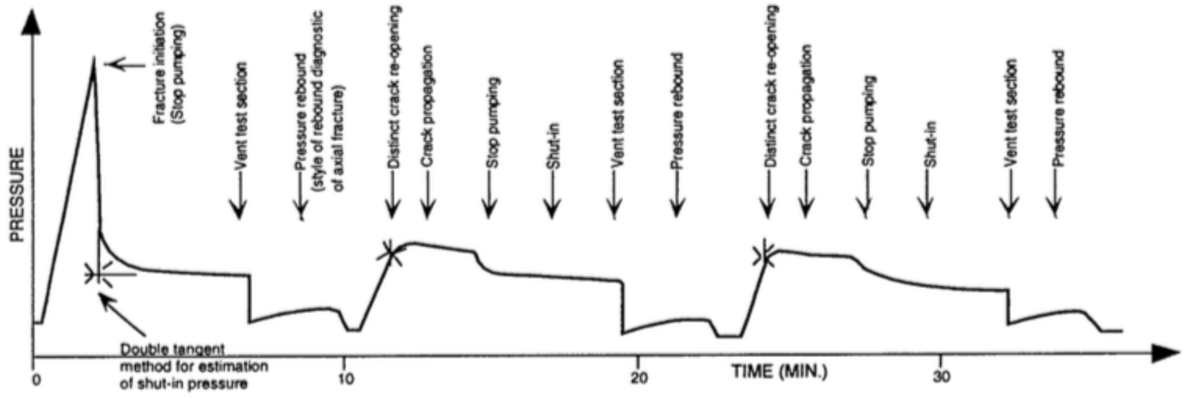

Figure 2.5: An ideal example of an ELOT, showing the pressure record and the wanted features. Copyright (Addis et al., 1998 Figure 3)

2.2.2 Quantifying Stress Changes

During injection or depletion of a reservoir the effective subsurface stresses will change due to pressure alterations inside the reservoir. This can be observed as surface subsidence and induced microseismicity, but not all fields will expose these phenomena. In the recent years, repeated seismic surveys have become a powerful tool to monitor the reservoir behaviour (Fjær et al., 2008). Today, time lapse-seismic can be helpful to evaluate the changes in fluid content, temperature and pore pressures in the reservoir as well as the stress changes in the subsurface.

It is however not straightforward to tie changes in the seismic response to the dynamic processes in the subsurface. In regard to stress estimation, the main challenge is that core measurements cannot be used directly when evaluating the actual, in-situ, case. The unloaded cores seem to be much more stress sensitive than the in-situ reservoir rock, most likely due to presence of microcracks caused by stress release during the coring process. This is observed in 4D data where the increase in wave velocities due to effective pressure increase is much smaller than the one predicted by laboratory experiments. The properties of the saturating fluid itself are also influenced by the pressure change, an effect that will counteract the change in velocity (Fjær et al., 2008). However, even if a reflector in a 4D survey only exhibits a time-shift, Δt, of a few milliseconds, this will in principle be enough to estimate stress changes in the subsurface (Garcia & MacBeth, 2013).

As shown in Section 2.1.2, time-strains can be transformed to physical strains using the relation $\frac{dT}{T} = (1 + R)\frac{dz}{z}$. The observed overburden strain vector, **d**, can be represented by a convolution of an unknown function, **f**, and the reservoir stress changes **m**.

$$\mathbf{f} * \mathbf{m} = \mathbf{d} \tag{2.34}$$

This can be redefined as an inverse problem by determining a Wiener filter $\mathbf{f_W}$ as an estimate for **f**. The reservoir volumetric strain distribution $\mathbf{m}'$ that might have caused an observed strain change in the overburden $\mathbf{d_{ob}}$ can now be found by convolving these data with the inverse filter $\mathbf{f_W}^{-1}$:

$$\mathbf{m}' = \mathbf{f_W}^{-1} * \mathbf{d_{ob}} \tag{2.35}$$

The volumetric strain can then be converted to mean effective stress by utilizing a simple linear relationship $\Delta\sigma = \kappa\varepsilon_{\mathrm{vol}}$, where κ is a porosity-dependent isotropic bulk modulus (Fjær et al., 2008). This is clearly a simple relationship, and the relation between strain deformation and effective stress might not be that straightforward in complex reservoirs (Garcia & MacBeth, 2013).

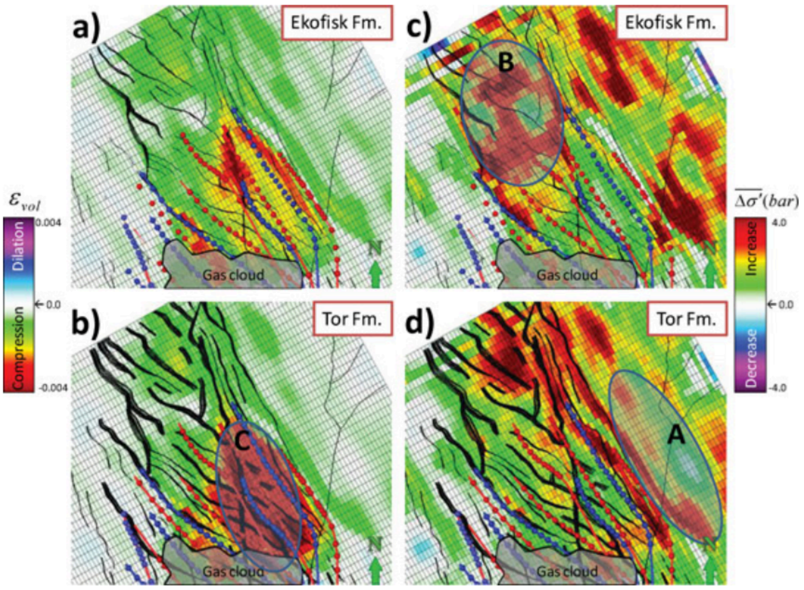

Figure 2.6: Estimated volumetric strain and mean effective stress change for the Ekofisk (a and c) and Tor (b and d) formations. Copyright (Garcia & MacBeth, 2013 Figure 11)

3 Induced Seismicity due to Hydrocarbon Production

There are several factors contributing to seismicity in the vicinity of hydrocarbon fields. Tectonic setting, existence of faults and the local stress regime all play important roles in the matter of seismic activity in an area, and they are factors that we cannot control. To be considered an induced seismic event, the underlying mechanism for the event will have to be man made. (J.-R. Grasso, 1992) presented three such mechanisms related to conventional hydrocarbon production which will be described further in this section: Injection of fluids to enhance the production rate or hydrocarbon recovery will lead to an increase in the pore pressure. The increased pore pressure will cause the effective normal stresses to decrease, and may cause pre-existing faults to slip following the Mohr-Coulomb failure criterion. Hydrocarbon depletion, on the other hand, causes the pore pressure in a reservoir to drop. This will affect the stress regime in the reservoir, and may even alter geological structures in and around the reservoir with seismic events as a by-product. The third main earthquake–inducing mechanism is related to the load removal due to massive hydrocarbon recovery. This may induce readjustments of the crust in the vicinity of the exploited field (J.-R. Grasso, 1992; Suckale, 2009).

3.1 Seismicity Induced by Pore Pressure Increase

Injection of water or gas in reservoirs is one of the most common stimulation methods in the petroleum industry. Massive fluid injection is done as a secondary recovery method in hydrocarbon reservoirs to maintain pore pressure and to sweep fluids from an injector well to producing wells. Fluid injection is also applied in order to stimulate reservoirs by creating new fractures and thereby increase the permeability, so-called hydraulic fracturing (Suckale, 2009). Hydraulic fracturing is closely linked with microseismicity, and this is an example where induced seismicity not necessarily is an unwanted phenomenon: By monitoring the induced microseismicity we can obtain important information about the fracture pattern and fluid movement in the reservoir (Maxwell & Urbancic, 2001). Microseismicity associated with hydraulic fracturing is well documented and discussed (e.g. Ilinski & Krasnova, 2010; Warpinski, 2013), and will not be described further in this thesis.

The basic mechanism behind the reactivation of faults or fractures due to fluid injection is well known and fairly intuitive: injected fluid enters the reservoir and will support part of the normal stress equivalent to the pore pressure of the fluid. This will lead to a reduction of the effective normal stress on the fault plane, and causes slip along pre-existing faults. This can be expressed as the Mohr-Coulomb failure criterion:

$$\tau = \mu(S_n - P_p) \qquad (3.1)$$

where τ is the shear stress on the fault, S_n is the normal stress, P_p is the pore pressure and μ is the coefficient of friction (Zoback & Zinke, 2002). Note that the frictional resistance may also be lowered when a fluid enters the fracture, as fluids have no shear strength. This can make it possible for faulting to occur at a level of shear stress at which fault slip would normally not occur.

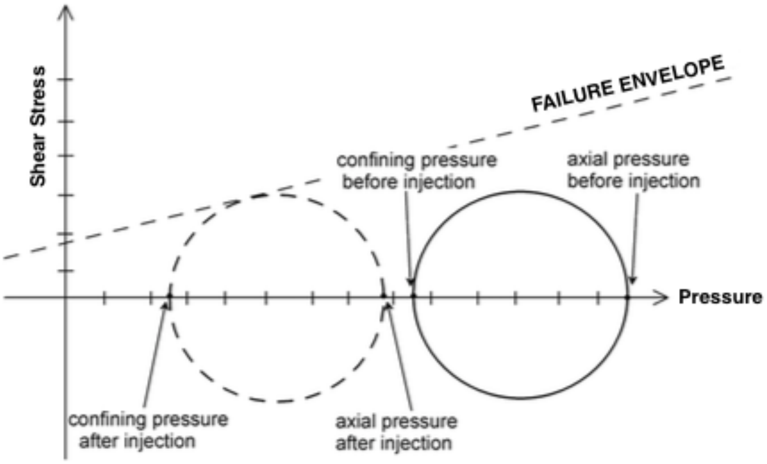

Figure 3.1: The effect of how fluid injection brings a rock closer to failure illustrated by a simple Mohr diagram. Copyright (Suckale, 2009 Figure 10)

(Raleigh, Healy, & Bredehoeft, 1976) tested if it was possible to control earthquakes in a reservoir in respect to the Mohr-Coulomb criterion through variation of fluid injection rates. An array of 14 short-period, vertical seismometers was installed at the Rangely Oil Field, Colorado, in 1969. Alternately injecting and recovering water from wells that penetrated a seismic active zone controlled fluid pressure in the reservoir. It should be noted that this was the first continuous seismic monitoring in the area, 12 years after waterflooding begun, thus no seismic background trend was available. Still, a correlation between seismicity and high pore pressures was established from analysis of the data from the microearthquake network. This result confirmed the predicted effect of fluid pressure on earthquake activity. The predictions were obtained by laboratory measurements of the frictional properties of the reservoir rocks, in situ stress measurements made near the earthquake zone and a Mohr-Coulomb type failure criterion.

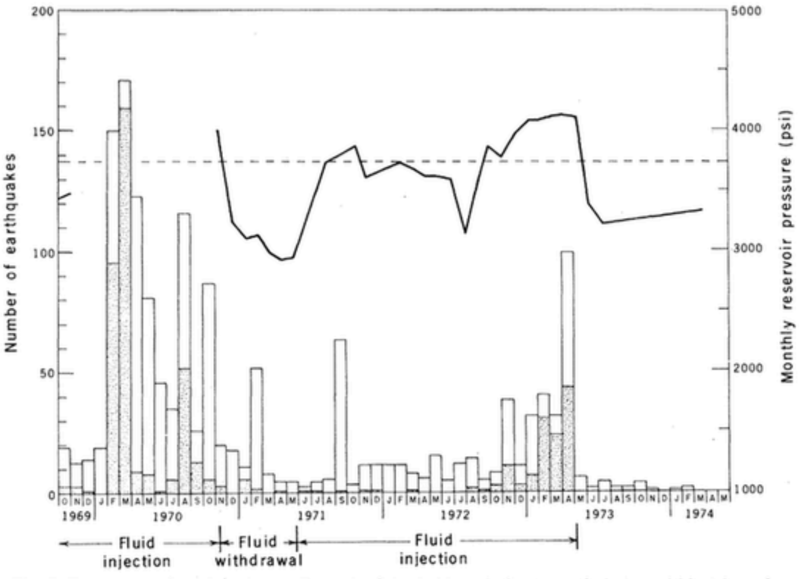

Figure 3.2: Correlation between earthquake frequency and pressure history at the Rangely oil field. Stippled bars indicate earthquakes within 1 km of experimental wells; the clear areas indicate all other events. The dashed line shows the predicted critical pressure.
Copyright (Raleigh et al., 1976 Figure 7)

However, this simple relationship between pore pressure and rock failure is not enough to directly explain all seismic events in a stimulated reservoir, especially not larger events. This was shown when a Mohr-Coulomb failure model was tested in the Cogdell Canyon Reef field by (Davis & Pennington, 1989). After an event in June 1978, with a magnitude of around 4.6, that was suspected to be associated with fluid injection, the U.S. Geological Survey carried out a seismic survey of the field. A total of 20 epicenters were located between 1979 and 1981. (Davis & Pennington, 1989) concluded that the Mohr-Coulomb failure model alone could not explain the activity because this would expect the events to be concentrated in areas of high fluid pressure, which was not observed. They argued that stress loading due to the weight of injected fluids might also be of importance to the investigated case, and that the seismic activity was a consequence of both increased pore pressure and stress loading.

3.2 Seismicity Induced by Fluid Extraction

That induced seismicity can be caused by fluid extraction may seem counter-intuitive given the arguments previously discussed. Depletion of a reservoir will reduce the pore pressure, and therefore increase the effective normal stresses working on a fault plane and thus prevent recurrent faulting in the reservoir. Still, evidence of extraction-induced earthquakes is unquestionably acknowledged. It is evident that the explanation for induced seismicity in producing reservoirs is much more complex than for fluid injections, and that geological setting must play an important role.

Seismic activity is not always observed inside depleted portions of a reservoir, but generally occurs in the surrounding rock mass. The seismic active regions in vicinity of the Lacq Field in southwestern France (Maury, Grasso, & Wittlinger, 1992) and the Strachan gas field in Alberta (Segall, 1989) are examples of this. (Segall, 1989) used poroelastic theory to investigate how extraction may promote induced seismicity in hydrocarbon fields. He modelled the connection between rock deformation and fluid flow to explain the induced stress in the rock mass surrounding a reservoir. Declining pore pressure can cause a producing reservoir to compact. Because the reservoir rocks are elastically coupled to the surrounding layers, this compaction will yield stresses in the neighbouring crust. Proof of this can be found in a number of fields throughout the world, where surface subsidence above producing reservoirs is observed and monitored.

The Ekofisk field is the largest chalk field in the North Sea. It was discovered in 1969 and is located in the Central Graben in the southern North Sea. At Ekofisk, seabed subsidence of more than 9 meters has been observed in the central part of the field since production started in 1971 (NPD, 2014). The overburden consists of under compacted weak shale and mud rocks and compaction of the reservoir due to increased effective stresses during fluid extraction is therefore transferred almost instantaneously to the seafloor as subsidence (Ottemöller, Nielsen, Atakan, Braunmiller, & Havskov, 2005). In 1984, a subsidence rate of 0.4 m/yr was discovered in the field, and it was decided to start water injection in order to re-pressurize the reservoir. Water flooding started in 1987 and was expanded in 1992, and has caused the subsidence rate to drop significantly. It should be mentioned that water was also unintentionally injected into the overburden which, according to (Ottemöller et al., 2005) and (Zoback & Zinke, 2002), triggered an earthquake with M_W=4.1-4.4 in agreement with the Mohr-Coulomb failure criterion.

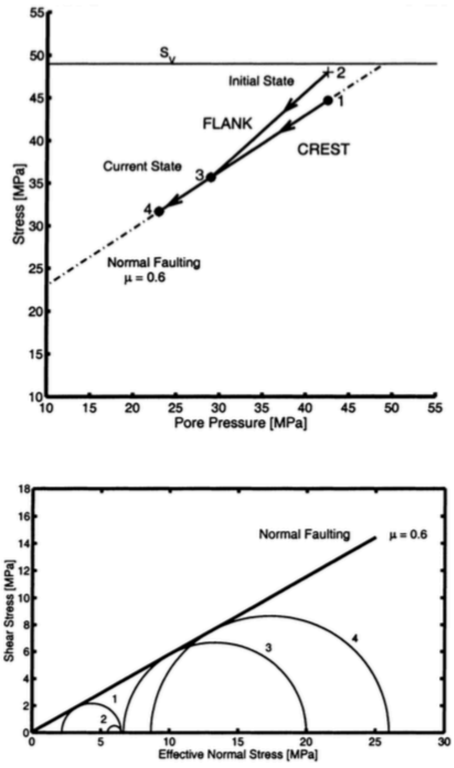

Figure 3.3: Relationship between initial stress states on the flank (state 1) and crest (state 2) of the Valhall Oil Field and their stress path during depletion. The lower figure is a Mohr diagram representation of the stress states. Note that the flank of the reservoir was not initially in a state of normal faulting, but this was induced by the depletion. Copyright (Zoback & Zinke, 2002)

As described in Section 2.1.2, (Segall et al., 1994) successfully computed a poroclastic model to simulate stress- and deformation fields in the Lacq field. However, this model failed to explain the location of many of the shallow induced earthquakes that had been registered in the area since 1969. (Segall et al., 1994) were though able to conclude that changes in effective stress in the overburden as small as 0.1 MPa were sufficient to induce earthquakes. Furthermore the tectonic stresses unquestionably had a huge impact on where seismic events would occur. Detailed in situ measurements for the entire area were not available, and this could explain why the model failed to predict the geometric location of many of the events. A later study done by Bardainne et al. (2006) concluded that some of the seismicity in vicinity of the field is likely due to fluid injection, according to (Suckale, 2009); (Segall et al., 1994) marginalized this effect in their study.

3.2.1 Seismicity Induced in Faulted Reservoirs

If pre-existing faults are present inside, or in immediate contact with, the reservoir, a different mechanism may explain the connection between fluid extraction and the induction of earthquakes. The basic idea is that increased effective normal stress acting on a pre-existing fault due to a pore pressure drop can increase the strength of the fault. This will thus create a barrier to slip in the area of the fault where fluid is extracted, and along these locked portions stresses can build up. It is observed that up to 90% of the deformation in a rock under stress is aseismic (Hazzard & Young, 2004). This can mean that in an apparent seismic inactive field, great stress can build up along such a locked portion of a fault either due to differential compaction or continued aseismic slip of nearby portions of the fault. As the pore pressure continue to decrease, the accumulated stress will eventually exceed the strength of the fault and induce an earthquake. (Pennington, Davis, Carlson, DuPree, & Ewing, 1986), who suggested this model, stresses that this process will repeat itself as long as the fault is active and fluid extraction continues, and that the magnitude of earthquakes is expected to increase over time. The theoretical limit on the size of an induced earthquake will in this model be determined by the size of the fault, the pressure drop and the mechanical properties of the rock matrix (see Section 4.1.3). They argued that this model could account for the seismicity observed at the Imogene and Fashing fields in Texas. These fields are characterized by structural traps of normal faulted limestones and were known to be seismically active, generating seismic events of magnitudes <4. A later study by Davis et al. (1995) concluded that the moderate events in the area around the two fields indeed were induced by fluid extraction as (Pennington et al., 1986) had suggested.

3.3 Seismicity Induced by Mass Transfer

In addition to pressure decrease due to depletion, complex fluid manipulations may be taken into account when evaluating induced seismicity related to both extraction and injection of fluids. In certain fields, where fluid injection is executed to sweep oil and gas to the producing well, seismic activity is observed between the depleted zone and the injection-receiving zone (J.-R. Grasso, 1992). It is believed that the combination of increased pore pressure and poroelastic stress transfer during water injection generates fractures. (Izadi & Elsworth, 2014) argues that also thermal and chemical strains drive the induced seismicity, but it is assumed that these effects contribute on a much smaller scale. Major earthquakes suspected to be related to hydrocarbon production includes three events in the vicinity of Coalinga, California, and the Gazli Earthquake Sequence in Uzbekistan. These events are all deep, mid-crustal earthquakes that cannot be explained solely by the mechanisms previously described.

The Coalinga earthquake in 1983, with magnitude M_S=6.5, was located 35 km north of the San Andreas Fault Zone in an area that had previously only exhibited scattered seismicity. The depth was estimated to around 10km, and its proximity to two major oil fields started speculations weather it might be related to production. The U.S. Geological Survey later ruled this out after initiating a detailed study of the event (Suckale, 2009). This report concluded that the shale units that underlie the oil-producing horizon have extremely low permeability and must be considered to hydraulically isolate the fields. Thus a poroelastic approach failed to explain the event, and it was proposed that a concealed fault zone along a structural boundary beneath the fields was closely associated with the earthquake.

After the occurrence of two other similar events in vicinity of Coalinga, a M_S=6.1 event beneath the Kettleman North Dome Oil Field in 1985 and a M_S=5.9 event beneath the Whittier Narrows Field in 1987, (McGarr, 1991) pursued a new model to explain all three events. He related the earthquakes directly to the produced volumes of oil and water. He argued that the removal of load induced by heavy fluid extraction would reduce the average density of the upper crust. This could in turn cause an isostatic imbalance of the crust that would result in an increasing load on a seismogenic layer and might trigger earthquakes. The three oil fields in question were all located in anticlines subjected to uplift due to horizontal compaction of the crust. (McGarr, 1991) proposed the following mechanical relationship between production and the earthquake sequence:

$$\Sigma M_0 = \frac{2\mu \Delta m \gamma}{\rho_c} \tag{3.2}$$

where ΣM_0 is the sum of the seismic moments, μ is the modulus of rigidity, Δm is the mass of the fluid removed due to oil production, γ is the fraction of the upper crust that is seismogenic, and ρ_c is the average upper crustal density.

This load removal model has later been considered as a trigger factor for the heavily debated Gazli earthquake sequence: The giant Gazli Gas Field is located in western Uzbekistan, which was considered to be an aseismic region until a destructive earthquake with a magnitude of M_S=7.0 marked the start of an unusual earthquake sequence. Two events of similar magnitude and tens of medium sized earthquakes followed the next eight years (Suckale, 2009). The producing reservoir is located at 2 km depth, while the depths of the earthquakes range from 5-20 km clustered around the reservoir. The sequence caused major structural damage in the area, but the exact location and rupture kinematics of the events remains debatable. Water had erratic been injected into the reservoir, and this would counteract the gas extraction in terms of mass removal. The region in which the Gazli field is located is continuously uplifted, and from an apparent 90 km migration of the seismicity in 10 years the possible existence of an immature fault zone has been interpreted. Thus, some has considered the resulting mass removal effect neglectable compared to tectonic mechanisms. Other studies have concluded that the gas field operations indeed have impacted the seismic activity in the area, and the relation between production and seismicity remains disputed (Suckale, 2009).

4 Earthquake theory

4.1 Magnitudes of Earthquakes

It is normal to measure the strength of earthquakes either based on the magnitude or intensity of the event. Intensity is related to the reactions of people or damage on buildings (Day, 2012) and will not be emphasized further as this is not very relevant for this thesis. There are several earthquake magnitude scales being used today, and the three most popular scales used by seismologists will be discussed in this section.

4.1.1 Local Magnitude Scale M_L

Professor Charles Richter from the California Institute of Technology developed the local magnitude scale, often referred to as the Richter magnitude scale, in 1935. Historically this is the most used and best-known scale for determination of earthquake magnitudes, and is calculated as follows (Day, 2012):

$$M_L = \log A - \log A_0 = \log \frac{A}{A_0} \tag{4.1}$$

where M_L is the local magnitude, A is the maximum trace amplitude and A_0 is a fixed minimum amplitude of 0.001 mm (which corresponded to the smallest detectable earthquakes at the time).

The maximum trace amplitude, A, should be the amplitude recorded by a standard Wood-Anderson seismograph with a natural period of 0.8 s, a damping factor of 80%, a static magnification of 2800, and located at a firm ground at a distance of exactly 100 km from the epicentre of the earthquake (Day, 2012). The local magnitude scale was originally constructed as an easy method to determine the size of earthquakes in California by using an amplitude-versus-range relationship defined specially for the geographic area and with a seismograph that is not longer in use. Still, the scale is still being used through filtering of modern broadband data and is important because all subsequent scales are tied to it (Shearer, 2009).

4.1.2 Surface Wave Magnitude Scale M_S

The surface wave magnitude scale was proposed by Beno Gutenberg and Richter in 1956, and is defined as follows (Day, 2012):

$$M_S = \log A' + 1.66 \log \Delta + 2 \tag{4.2}$$

Where M_S is the surface wave magnitude scale, A' is the maximum ground displacement given in micrometres, and Δ is the epicentral distance to the seismograph measured in degrees.

This scale is based on amplitude of surface waves with periods of about 20 seconds, and its advantage is that it may be calculated using any kind of seismograph. The distance from the epicentre to the seismograph should though be at least 1000 km, and the earthquake should preferably have a shallow depth.

4.1.3 Moment Magnitude Scale M_W

The moment magnitude scale is the most commonly used magnitude scale today, especially for larger earthquakes. The two seismologists Hiroo Kanamori and Thomas C. Hanks proposed the scale in 1979 by the following equation:

$$M_W = -6.0 + 0.67 \log M_0 \qquad (4.3)$$

Where M_W is the moment magnitude, and M_0 is the seismic moment given by:

$$M_0 = \mu A_f D \qquad (4.4)$$

μ is the shear modulus of the material along the fault plane, A_f is the area of fault plane that is undergoing slip, and D is the average displacement of ruptured segment of the fault. The seismic moment is determined from a seismogram using very long-period waves so that even a fault with a very large rupture area appears as a point source (Day, 2012).

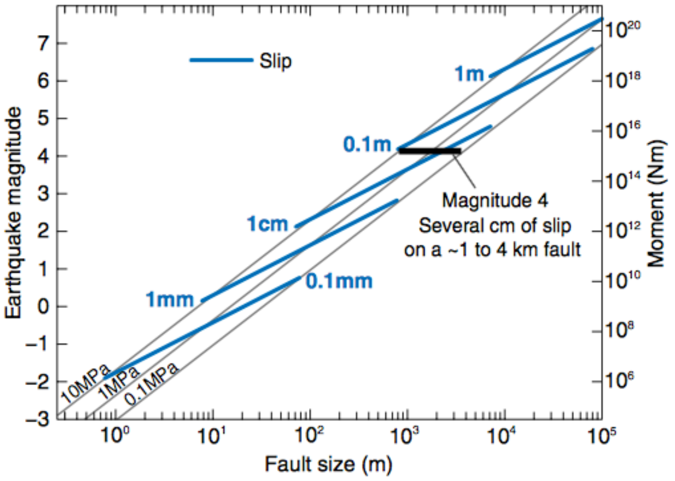

Figure 4.1: Relationships among various scaling parameters for earthquakes. Note the significance of the amount of slip. Copyright (Zoback & Gorelick, 2012)

4.1.4 Comparison of Magnitude Scales

Figure 4.2 shows an approximation of the relationship between different magnitude scales. It is clear that the scales deviates from each other at high values. The “saturation” of the different scales is related to the fact that they will not be able to distinguish the size of large earthquakes solely on the amplitude recorded on the seismogram (Day, 2012). The three scales previously discussed are reasonably close to each other, at least for magnitudes <7. For this reason, the different scales may be used sporadically in scientific papers, as well as in this thesis.

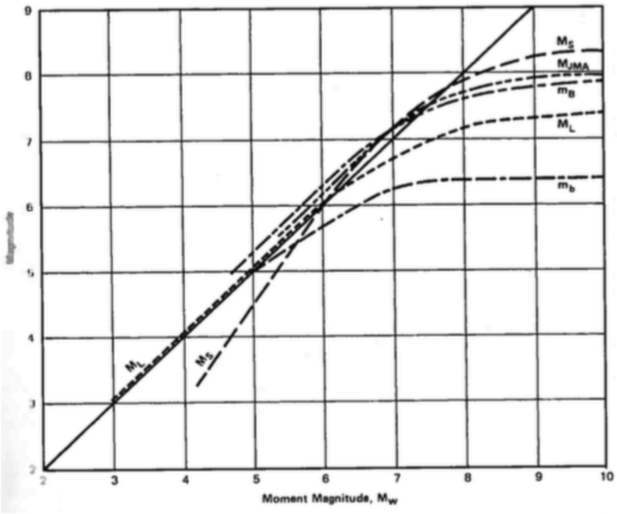

Figure 4.2: Approximate relationships between the moment magnitude scale M_W and other magnitude scales. Copyright (Day, 2012 Figure 2.15)

4.2 Occurrence

Even though seismicity in vicinity of hydrocarbon fields is not a rare phenomenon, it is not straightforward to determine weather or not these events occur naturally or are induced. It should also be mentioned that not all fields have been monitored for seismicity and therefore minor seismic events may have taken place undetected, and that in some cases natural seismicity can obscure the induced events. Over the past decades many case studies have been carried out, and for some hydrocarbon fields a connection between human activity and seismic events are agreed upon while for others the conclusions are debatable or controversial.

(Perrodon, 1983) states that out of the roughly 600 sedimentary basins worldwide, 160 are used for commercial hydrocarbon production. For most basins, minimum 80% according to (J.-R. Grasso, 1992), most of the local deformation is considered aseismic. Only a handful of basins show frequent incidents of induced seismicity, and within these basins the hydrocarbon fields are not necessarily similarly affected (Van Wees et al., 2014). The reason for this is not fully understood, but extensional studies have been done to determine the key parameters for the observed seismicity (e.g. Van Eijs, Mulders, Nepveu, Kenter, & Scheffers, 2006).

4.3 Monitoring of Induced Earthquakes

In relation to induced seismicity in the petroleum industry, earthquake monitoring is of upmost importance in order to improve our understanding of the seismic activity in the vicinity of hydrocarbon fields. The explosion of unconventional production methods and the ongoing development of geothermal energy exploitation have contributed enormously to the passive monitoring of microseismicity, as small magnitude microearthquakes is used directly to map the fracture growth during hydraulic fracturing of reservoirs (Maxwell & Urbancic, 2001). With respect to monitoring of conventional reservoirs the time-lapse seismic practitioners are the strongest initiative takers. Permanent deployment of geophones on the sea bottom is an expensive investment, but an increased focus on Enhanced Oil Recovery (EOR) has encouraged the petroleum companies to use 4D seismics to monitor fluid movements and to pinpoint unproduced parts of reservoirs (Bjørlykke, 2010). In some special cases geophones on the ocean bottom surface will be able to pick up microseismicity in a reservoir, and for these cases it would be possible to utilize the seismic sensors to monitor microseismic events in the periods between the conventional seismic surveys. However, in general, passive monitoring will usually involve borehole arrays due to the need to keep the instrumentation close to the seismic activity in order to maximise sensitivity (Maxwell & Urbancic, 2001). Microseismic monitoring is generally carried out the same way as earthquake monitoring, but on a smaller scale.

Recording of passive seismic data can give us important information about reservoir dynamics, and is associated with stress changes in an around the reservoir. In addition to hydraulic fracturing, as previously mentioned, the most relevant application of passive monitoring in hydrocarbon fields are, according to (Suckale, 2009) and (Maxwell & Urbancic, 2001):

- Well and casing design: Microseismic activity is related to rock mass deformations that can cause well failure. In the Valhall Field, as well as in the Cold Lake Field, microseismic monitoring identified microseismic activity in the overburden. This activity was attributed to shear deformation of the overburden that could cause well failure.

- Fault mapping: Movements of fault systems can be detected by using microseismic monitoring. This was successfully done in the Ekofisk Field, when the fault pattern under a gas cloud was identified during a 18-days microseismic survey.
- Mapping fluid movements: Microseismic activity can be related to pressure changes due to fluid movements in a reservoir. Fault activation at the Seventy-six Oil Field in Kentucky was detected by microseismic monitoring and was suspected to be caused by water inflow to the producing reservoir. This was confirmed with data from well logs, drill tests and production history.
- Mapping compaction strains: Microseismic data from the Ekofisk as well as the Lacq fields have been related to strains associated with compaction of the reservoirs. This can be used to investigate cap-rock integrity and to verify geomechanical assessments of compaction.

A limited number of studies on permanent measuring of passive microseismicity have been carried out in conventional hydrocarbon fields, and these have usually been executed in the relatively few fields where seismic events are felt on the surface. As previously mentioned, microseismic events are normally not strong enough to be recorded on the surface and instruments will have to be placed closer to the source. Even tough the technology to do this exists, e.g. wireline arrays capable of recording small amplitude data, microseismic monitoring is still not commonplace in the industry (Maxwell & Urbancic, 2001). One reason for this is the enormous amount of data that accumulates throughout a passive seismic survey.

5 Earthquake Prediction

Earthquake prediction has been researched for more than 100 years, apparently with no obvious success. Many ideas for prediction of earthquakes have been explored, but reliable prediction is not possible on any time scale today (Shearer, 2009). The subject of earthquake prediction has lately gained worldwide attention after an Italian court sentenced six scientists and a government official to six years in prison for manslaughter for giving false assurances before a devastating earthquake that hit the city of L'Aquila in 2009. The event shocked the world's scientific environment, even though the verdict was overturned in November 2014 (Hooper, 2014).

One of the most studied fault systems in the world is the infamous San Andreas Fault Complex in California. This right-lateral strike-slip fault zone marks the plate boundary between the Pacific Plate and the North American Plate and has induced several catastrophic earthquakes the past centuries (Shearer, 2009). Many scientists argue that the larger events (M>8) in the fault system may show a periodic behaviour, and this is a widespread idea in the world today. However, earthquakes of these magnitudes on particular faults may have a time spacing of hundreds of years which makes it very difficult to support this theory with certainty using data catalogues. It should also be mentioned that paleoseismologic surveys, e.g. from the San Andreas Fault System described in (Grant & Lettis, 2002), fails to demonstrate a regular recurrence interval. This has been used to support the theory that slip on faults represents a chaotic system, and that long-term earthquake prediction thus is fundamentally impossible (Shearer, 2009). This being said, a successful earthquake prediction was made in China in 1975 when the city of Haicheng was evacuated prior to a magnitude 7.3 earthquake. 90% of the buildings in the city were destroyed, but due to the evacuation very few people were killed. The prediction of the Chinese seismologists was based on a number of observed phenomena, including animal behaviour, groundwater anomalies and a highly unusual foreshock in the generally seismic inactive region.

The earthquake prediction models that have been explored range from simple strike-slip spring models to delicate statistical models for complex fault systems. The apparent lack of any obvious precursor prior to such incredibly powerful events as a major earthquake has been a mystery to scientists since deployment of instrumentation started (Shearer, 2009). The processes underlying earthquakes are still not fully understood. However, (Bak & Tang, 1989) and (Sornette & Sornette, 1989) proposed a self-organized critical model for rationalizing observations on occurrences and magnitudes of earthquakes that should be investigated further.

5.1 The Theory of Self-Organized Criticality

In the latter part of the 1980's, Per Bak, Chao Tang and several other associates from the Brookhaven National Laboratory introduced the theory of self-organized criticality (SOC) in a series of papers (Bak, 1997). The basic physical model for SOC is a sand pile where sand grains are added continuously. The pile will grow over time, and the angle of the slope will increase until it reaches an angle close to the maximum angle of repose. Additional grains will then trigger slides of different sizes on the slope, but it is difficult to predict which grains will cause the largest slides. The system has evolved naturally towards a stationary self-organized critical state, with no length or time scale other then the ones deduced from the size of the system itself. This simple model was first suggested to represent the underlying mechanism for the widespread occurrence of 1/f-noise, which is a source of considerable interest in many fields (Bak, 1997), but has been applied to a number of scientific disciplines over the last decades. This includes earthquake research, where the existence of 1/f noise is observed in the time gap between large earthquakes (Sornette & Sornette, 1989). In addition to 1/f noise, the emergence of the self-organized critical state connects nonlinear dynamics and the appearance of spatial self-similarity in a natural and robust way (Bak, Tang, & Wiesenfeld, 1987). By considering the displacement and fracturing of rock mass in fault zones upon applying increased stress, it is clear that earthquakes indeed show nonlinear behaviour.

(Bak et al., 1987) demonstrated that SOC systems will provide a power-law relation between frequencies and sizes of events. Richter and Gutenberg acknowledged this relation in earthquake study already in 1944, when they proposed a statistical relation between the magnitude and number of observed seismic events. Ishimoto and Iida published a similar result in 1939 (Hough, 2007), but still this relationship is known as the Gutenberg-Richter law:

$$\log N = a - bM \tag{5.1}$$

Here a and b are constants that may depend a little upon the region of observation, but still the law is regarded as remarkably universal and makes a good fit both on a local and global scale, especially for earthquake magnitudes <6.5 (Sornette & Sornette, 1989).

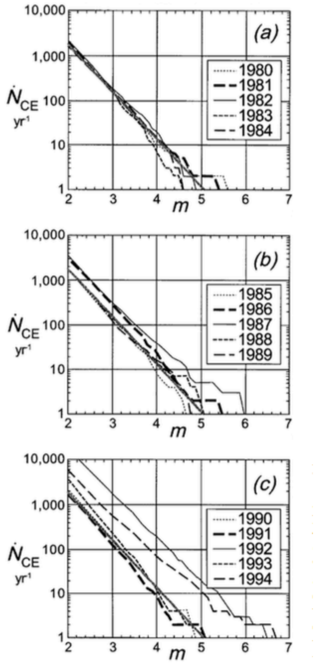

Figure 5.1: Cumulative number of earthquakes per year, $\dot{N}_{CE}$, with magnitudes *m* occuring in southern California between 1980 and 1994. The heavy straight lines in (a)-(c) represents the best fit to all data, the Gutenberg-Richter relation (Equation 5.1), with *b*=1.05 and $\dot{a}=e^{a}=2.06*10^{5}$ per year. Copyright (Turcotte, 1999)

The idea of considering the crust to act in a self-organized critical way is today well acknowledged (e.g. Bak, 1997; J. R. Grasso & Sornette, 1998; Sornette & Sornette, 1989 and more) and is still gaining popularity. Slider-block models, which have been used as an analogue for earthquakes since the 1960's, has been demonstrated to exhibit SOC (Malamud & Turcotte, 1999). A wide variety of slider-block models have been proposed, but the basic principle is that slider blocks are pulled over a surface by springs attached to a plate moving with constant velocity *v*. The blocks are coupled to each other with connector springs, and the interaction of the blocks with the surface is controlled by friction. The simplest friction law to describe the behaviour is the static-dynamic friction law: If v=0 the static frictional force is F_s, but when the plate moves the dynamic frictional force is F_d. If $F_s > F_d$ stick-slip behaviour is obtained, and the motion of the blocks is characterized by periodic slip events (Turcotte, 1999). Similar to a slide in the sand pile model, these slip events appear to be unpredictable and occurs randomly (Malamud & Turcotte, 1999).

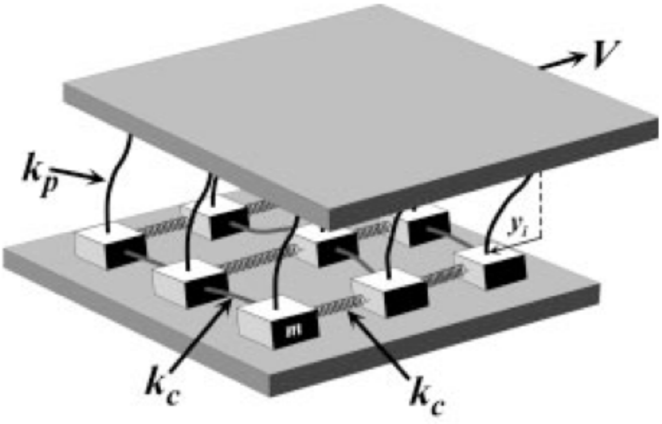

Figure 5.2: Illustration of a two-dimensional slider-block model. Each block with mass *m* is coupled to neighbouring blocks with connector springs with spring constants k_c, and to a driver plate moving at constant velocity, *V*, with springs with spring constant k_p.
Copyright (Malamud & Turcotte, 1999 Figure 6)

(McLaskey & Glaser, 2011) developed this slider-block model further, and performed strike-slip experiments on interfaces of plastic/plastic and rock/rock and recorded the induced nano earthquakes with an array of nanoseismic sensors. These experiments presented events that seemed fairly representative of tectonic earthquake behaviour.

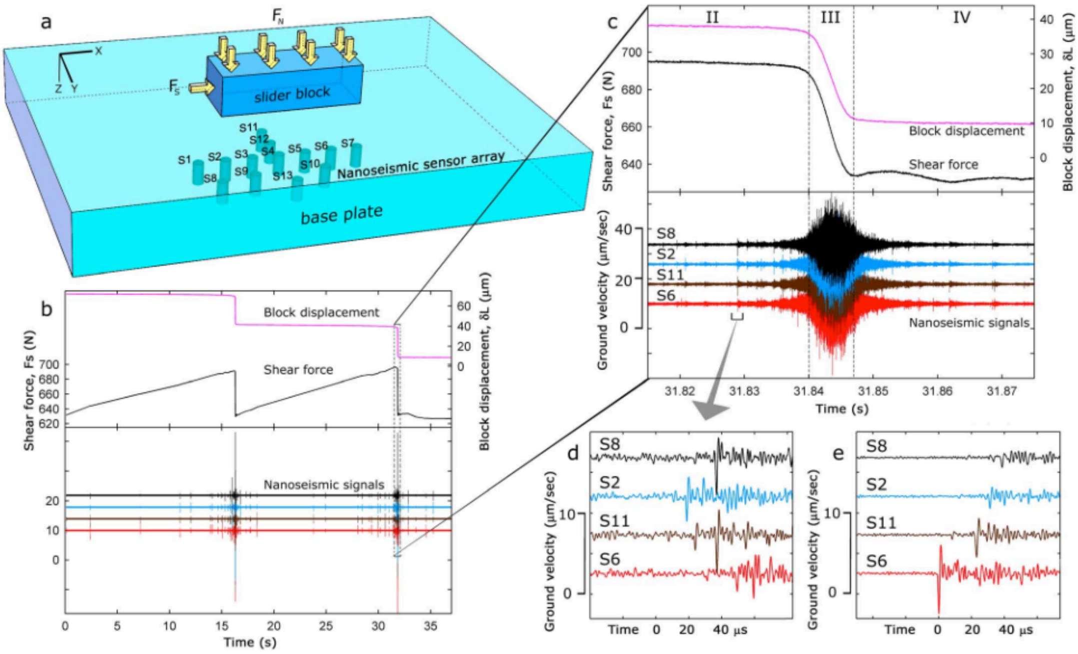

Figure 5.3: Schematic diagram of McLaskey and Glasers stick-slip experiment and typical results for a rock/rock interface. (a) Illustration of the model. (b) Shear force and slider block displacement for two full stick-slip cycles along with acoustic log. (c) Detailed view of a stick-slip instability that shows that the recorded signals consist of a multitude of discrete events. (d, e) Single events shown in detail illustrating rapid P- and S-wave arrivals. Figure (5.3e) is from an "aftershock" event occurring 0.2 seconds after the slip instability shown in (5.3c). Copyright (McLaskey & Glaser, 2011)

If the theory of SOC holds it may help us understand why apparently marginal stress changes in the subsurface due to production or injection can cause earthquakes. It also raises the question of why induced seismicity is not present everywhere. (J. R. Grasso & Sornette, 1998) argues that it is fundamentally wrong to consider the entire crust as a SOC system. In fact, most of the crust is relatively stable and therefore resistant to small stress changes. The rich variability of the Earth's crust is far to complex to be captured in a single model, and SOC should only be evaluated in suitable areas.

6 The Groningen Field

Before the drilling of the Slochteren 1 well in 1959, the target formations around the Netherlands were mainly confined to Permian Zechstein carbonate rocks and Triassic Bunter sandstones onshore of northern Germany and the eastern Netherlands. The first exploration well in the province of Groningen, Haren 1, was drilled in 1952 targeting the Zechstein Formation due to gas discoveries in Germany, near the Dutch border, in this formation. The well was drilled deeper, and became the first to penetrate around 180 m of the Lower Permian Rotliegend Group. The Rotliegend Group was water-bearing, but proved the presence of a potentially important reservoir underlying the shallower evaporitic sequences. The discovery of gas-bearing Rotliegend sandstones by the Slochteren 1 well led to intensified exploration in the region at deeper depths and many new discoveries. Additional wells, improved velocity models and detailed seismic mapping around Groningen proved that previous interpretations of isolated structures and anomalies were actually part of one massive gas field.

6.1 Geological Background

The geological history of the Netherlands, including the Groningen field, is fairly well documented and understood. Subsurface exploration in the area started more than 100 years ago, and to this date more than 4000 deep wells on- and offshore the Netherlands have penetrated Permian strata. Around 55% of the country has also been covered by 3D seismic surveys (Geluk, 2005).

The depositional history of the Netherlands has been controlled by three orogenic phases since late Carboniferous time, namely the Variscan-, the Cimmerian- and the Laramide tectonic phases. The Anglo-Dutch Basin developed in the Variscan Foreland, where deposits were derived from a mountain range in the south of the Netherlands. Carboniferous sediments contain large amounts of coal (e.g. Westphalian coals), and sedimentary facies consist of alternating deltaic sandstones and shale. Gas in the Groningen Field is sourced mainly from the Westphalian Coal Measures, which dictates most of the hydrocarbon distribution in the area. The marine intercalations become less important upwards in the Anglo-Dutch Basin, and gradually change into continental redbed facies without coal. In the Groningen area, however, these redbeds are not present, either due to lack of deposition or because they were removed during uplift and erosion associated with the late Variscan tectonic phase. The period of non-deposition is known as the Saalian Unconformity in the Netherlands, separating the Upper Carboniferous from Permian aged Rotligend Group sediments. In the eastern parts of the

South Permian Basin, which stretches from eastern England to the Russo-Polish border, several other unconformities are recognised, but these merge into a single unconformity westwards (Doornenbal & Stevenson, 2010). (Doornenbal & Stevenson, 2010) suggested the name Base Permian Unconformity (BPU) for this mega-unconformity separating the Carboniferous sediments from the Lower Permian Rotliegendes Group (Figure 6.1). Towards the end of the Carboniferous the regional stress pattern changed dramatically, from the compressional regime associated with the Variscan Orogeny to an extensional regime subsequently followed by regional uplift in the Early Permian (Doornenbal & Stevenson, 2010).

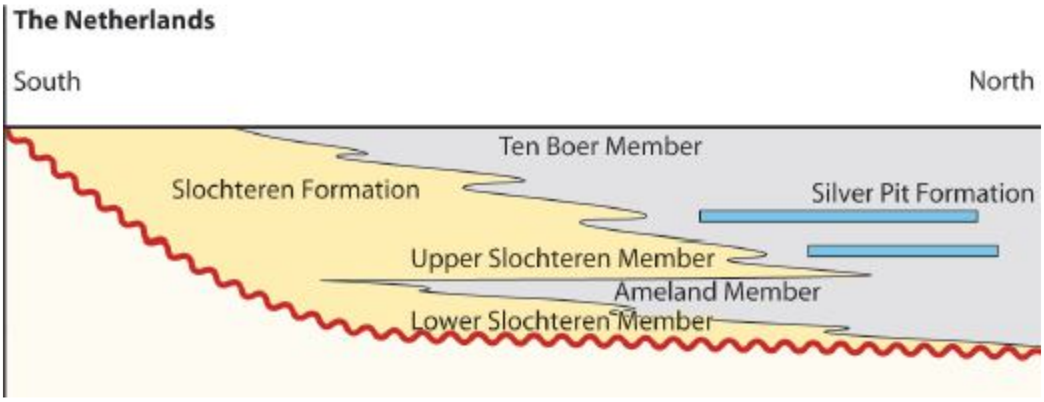

Figure 6.1: The Rotliegend tectonostratigraphic chart, based party on Glennie (2007). BPU marked as hiatus. Modified from (Doornenbal & Stevenson, 2010 Figure 7.1)

The Rotligend Slochteren Formation is the first Permian sediments in the Groningen area deposited over the BPU. The Slochteren Sandstone may be divided into an upper and lower part: Fluvial conglomerates and sandstones dominate the lower part, while the upper part consists of well-sorted fine-grained aeolian sandstones alternating with claystones. Both parts were deposited during arid climatic conditions. The aolian sands are more prominent in the north where a decrease in the number of conglomeratic beds is also observed, therefore assuming a main clastic source area of the Rotliegendes Group to the south (Fig. 6.2). In the Groningen field the thickness of the Slochteren Sandstone increases from around 70 m in the south-east to 240 m in the north-west of the field (Doornenbal & Stevenson, 2010). Porosities range from 10% to 25% with an average of 17%, and the average permeability is 240mD. In the northern part of the Groningen Field a shale layer, the Ameland Claystone Member, divides the Slochteren Formation in an upper and lower part and acts as a barrier to fluid flow between the two units on a local scale. Extension during the early Permian led to synsedimentary faulting within the entire Upper Rotliegend Group (Bourne, Oates, Elk, & Doornhof, 2014; Geluk, 2005).

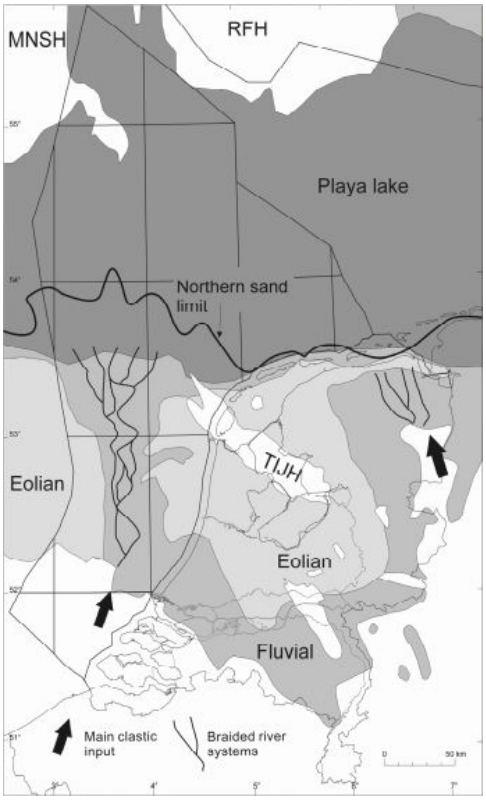

Figure 6.2: Map showing the overall facies distribution at the onset of deposition of the Upper Slochteren member. Arrows indicate the main fluvial feeder systems. Copyright (Geluk, 2005)

The uppermost massive sandstone unit underlying a continuous shale-dominated succession, the Ten Boer Claystone Member, defines the top of the Slochteren Formation. The Ten Boer Member consists predominantly of hard, silty, claystones with very low permeabilities interbedded with thin fine-grained sandstone and siltstone beds deposited in the Middle Permian. Ten Boer Member thicknesses range from some 30 m in the southern part of the field to 75 m in the north, acting as a regional seal (Rondeel, Batjes, & Nieuwenhuijs, 1996). This succession represents a change from arid continental deposition and erosion of the Slochteren Formation to restricted marine environments of the overlying Zechstein evaporites controlled by subsidence of the basin coupled with episodic marine incursions (Brouwer, 1972; Stauble & Milius, 1970).

An Upper Permian marine transgression marks the start of the Zechstein evaporite series, and resulted in the deposition of a thin bituminous claystone, the Copper Shale, conformably above the Upper Rotliegend Ten Boer Member. The Zechstein Group in the Groningen area consists of five evaporite cycles. The thickness of the salt and carbonates varies greatly due to salt movements, but the average thickness is around 1 km (Figure 6.3). This thick package forms an effective top seal in the Groningen area as well as the rest of the South Permian Basin.

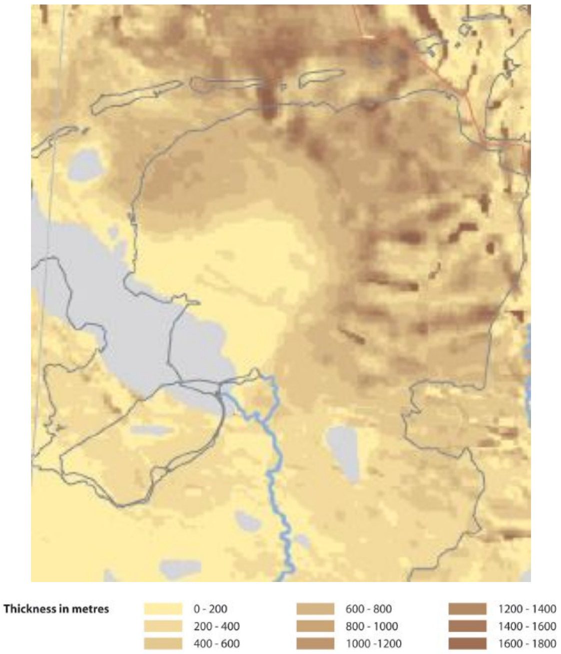

Figure 6.3: Thickness of the Zechstein in northern Netherlands. The Groningen field is located in the upper right corner. Modified from (Doornenbal & Stevenson, 2010 Figure 8.3)

Triassic rocks lie conformably on top of the Permian salt, but the younger stratigraphic units of the Triassic as well as Jurassic are not found in the Groningen area due to significant uplift associated with the Cimmerian tectonic phase during the Jurassic (Doornenbal & Stevenson, 2010; Stauble & Milius, 1970). This tectonic phase shaped the Groningen High, which is a stable structural high bounded by the Lauwerszee Trough to the west and the Ems Graben to the east. Uniform sedimentary conditions were not restored until the Late Cretaceous, when sediments were deposited above the Late Cimmerian Unconformity.

The reservoir units in the Groningen Field are located on the Groningen High at the depths of 2600 to 3200 m. The spatial extent of the field exceeds 900 km^2, making it the largest gas field discovered in western Europe with an estimated recoverable volume of about 2800 billion cubic meters of gas (Bourne et al., 2014). The Upper Rotliegend Slochteren Formation forms the main reservoir, but approximately 7% of the gas initially in place (GIIP) is found in the Limberg Group sediments of Carboniferous age, located below the BPU. To date, surface facilities in the field include some 300 active production wells, drilled from 29 clusters (Doornenbal & Stevenson, 2010).

6.2 Faults

More than 1800 faults have been mapped in vicinity of the Groningen Field (van Elk & Doornhof, 2012), and both fault density and fault strike are variable throughout the field. A complex interplay of dominantly NW-SE oriented dextral wrench tectonics and related ENE-WSW antithetic Reidel structures have been active in the NE Netherlands since Carboniferous time (Frikken, 1999). The faults were first formed during the Late Carboniferous to early Permian extensional phase, and can be seen in the Groningen Field Carboniferous strata underlying the BPU, and in synsedimentary fault movements observed in the Rotliegend Group (Bourne et al., 2014; Geluk, 2005; Stauble & Milius, 1970). Most of the latter fault populations were reactivated during an extensional phase from the Triassic to late Jurassic and during the Cimmerian tectonic phase. Reversal of the stress regime in the late Cimmerian phase, as well as the Laramide and the late Alpine orogenic phases also resulted in N-S to NNW-SSE compression and reactivation of the dextral wrench movements in the northeastern Netherlands. Halokinesis of the Zechstein Group during the Cretaceous will also have loaded the faults further. All faults in the proximity of the reservoir terminate in the incompetent and rheologically weak salt of the Zechstein Group, and subdivide the Groningen field into a number of fault compartments. A slight difference in free water level, reservoir pressure and gas composition have been observed although the overall communication between the compartments appears to be good (Doornenbal & Stevenson, 2010).

6.3 Seismicity

The south-eastern part of the Netherlands has historically been known to exhibit natural seismicity, with events reaching magnitudes up to M_W=5.4 (Van Wees et al., 2014). Normal faulting along NW-SE striking fault zones and NE-SW extension is the main cause for this activity. This extensional phase started during the Late Oligocene (ca. 25 Ma) and developed into the present-day structure that is observed in the Roer Valley Graben (Van Balen, Houtgast, & Cloetingh, 2005). The northern part of the Netherlands is characterized by a more tectonically stable regime. The basin compartments of the northern Netherlands are believed to be tectonically inactive, which is supported by the fact that no natural seismicity has been recorded in the area. In fact, there is no evidence of any seismic events in the northern Netherlands prior to an earthquake of magnitude M_L=2.8 recorded near the town of Assen in 1986. The shallow depth of around 1 km, coupled with its vicinity to a producing gas reservoir and the absence of any previous seismic activity in the region led to the conclusion that the event was induced by human activities (Van Eck, Goutbeek, Haak, &

Dost, 2006). Since then, more than 800 induced earthquakes with magnitudes $M_L<3.5$ have been registered in the Netherlands, with the majority of them in the northeastern part of the country, according to the Royal Dutch Meterological Institute (KNMI). Even though the earthquakes are relatively small in magnitude, the events are shallow in depth and occasionally cause non-structural damage to foundations and properties. This has led to growing concerns amongst the civilian population, regional governments and industry operators in the Netherlands, prompting a law instituted in 2003 that requires a risk and hazard analysis for all new exploitation licences (Van Eck et al., 2006).

In the Groningen Field, the first seismic event ($M_L=2.4$) was registered in December 1991, 28 years after gas production started. Since then, several hundred seismic events have been recorded within the lateral boundaries of the gas field. Following the onset of seismicity in the northern part of the Netherlands, seismic monitoring in the north was expanded in several phases. The first borehole seismometer was installed in 1992, followed by a complete monitoring network consisting of 19 permanent seismometers in 1995. This network was further upgraded in 2010 with the addition of six shallow borehole stations and the implementation of real-time continuous data transmission with automatic detection and location capabilities (Bourne et al., 2014). After the first event in the Groningen field in 1991 seismicity was quite stable, averaging at a rate of approximately five $M>1.5$ events per year (van Thienen-Visser & Breunese, 2015). However, in 2003 a clear anomaly to this apparent stationary seismicity was observed, both in terms of frequency and magnitude of events. This year was the first time a $M_L\geq3.0$ event occurred, while the number of earthquakes tripled compared to previous years. After 2003 this increase in frequency and magnitude has remained steady, and it has become more evident that seismicity in the area is a nonstationary and complex phenomenon. The largest event to date ($M_L=3.6$) occurred in 2012, and in the past five years the number of events has fluctuated between 19 and 29 per year (van Thienen-Visser & Breunese, 2015).

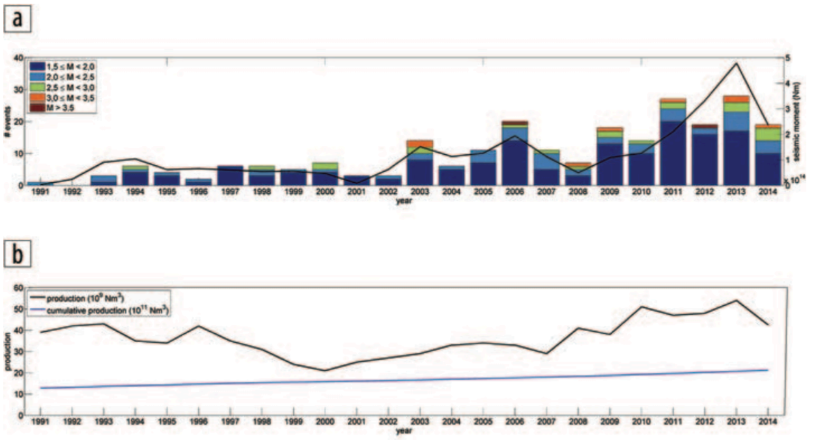

Figure 6.4: (a) Number and magnitude of events, and seismic moment, per year in the Groningen Field. (b) Yearly gas production and cumulative production from 1991 until 2014 (in normal cubic meters). Copyright (van Thienen-Visser & Breunese, 2015)

Even though precise mapping of the epicenters is hard to achieve due to sparseness of the monitoring array, it is assumed based on the successful tracing of a handful events that most of the seismicity occurs at reservoir depths (around 3000 m). An estimated 90% of the events also occurred at a time and place when reservoir compaction had increased 18 cm (Bourne et al., 2014).

Several underlying mechanisms for the induced seismicity in the Groningen field have been proposed and studied. Many of the events recorded in the Groningen field seem to occur at reservoir levels along pre-existing NW-SE trending faults. The number of events and their maximum amplitude also show a clear relation with production time (Van Eijs et al., 2006), as predicted by the model of (Pennington et al., 1986). (Van Eijs et al., 2006) made an attempt to determine why only a few of the on-shore gas fields in the Netherlands showed evidence of induced seismicity. Different controlling mechanisms were evaluated based on observations made at 16 fields known to produce induced seismicity at the time, and three key properties that could be used to predict seismicity in producing fields were established. (Van Eijs et al., 2006) concluded that pore pressure reduction is the dominating driving force for the induced events, and the stiffness contrast between reservoir and sealing rock and the local fault density were the other two key parameters that determine the existence of induced seismic events. Based on these three parameters they evaluated the probability of induced seismicity in all producing fields in the Netherlands. For gas fields where the pressure drop would not reach a critical value of 72 bar throughout their production time, the probability of future seismicity was set to zero. As of 2014, none of these fields had shown any sign of seismicity (Van Wees et al., 2014).

More recently, (Bourne et al., 2014) developed a seismological model for earthquakes induced by subsurface reservoir volume changes. They calibrated a compaction model, expressed as a function of spatial position and time since production start, for the Groningen field using various geodetic data and expressed the available seismic moment in terms of the volume change. In this way probability density maps for earthquake locations can be calculated from the compaction maps. They concluded that the preferential location of the seismicity in the central part of the field does not correlate with the prominent uniform pressure distribution caused by the good connectivity in the field. Instead, they observed that the seismicity pattern correlates very well with the pattern of compaction, which is dependent on the thickness and compressibility of the reservoir rock as well as the pressure depletion.

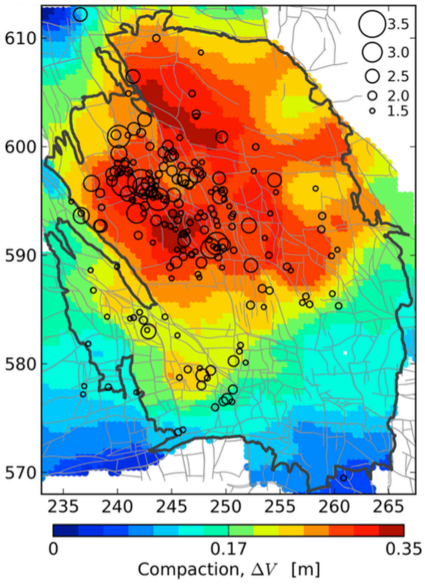

Figure 6.5: Earhquake epicenters in the Groningen Field from 1995 to 2012 in relation to a reservoir compaction model from 1960 to 2012. Note that most events are located in areas with significant compaction. Copyright (Bourne et al., 2014)

6.4 Subsidence

Surface subsidence is a big concern for the public and authorities in the Netherlands due to the low altitude of the country. Almost 20% of its area consists of reclaimed land situated below the mean sea level, and the country is thus very vulnerable to sea level rise and land subsidence. The most prominent example of this is the infamous storm tide 1st of February 1953 when a number of dikes in the south-western Netherlands collapsed which resulted in a dreadful flooding killing 1800 residents (Rietveld, 1986). Levelling surveys have been executed in the country for hundreds of years, with the oldest measurements dating back to the 16th century. In the Groningen field, precision levelling surveys have been conducted regularly since production started in 1963. The first campaign, in 1964, was carried out in the southern part of the field, but in 1972 the monitoring network was extended to the entire field, covering around 900 km^2. Benchmark density was also increased at this time, and further improvements were done in 1987. Today, also GPS- and InSAR measurements are used to monitor the subsidence bowl around Groningen in addition to the optical levelling technique that has been used since 1964. Also formation compaction monitoring using radioactive bullets in deep observation wells has been carried out in the Groningen field. The radioactive marker technique was originally developed for the field, and the first testing of the method and equipment was carried out already in 1968. Acquisition of reasonable compaction data has been performed since 1974 (Mobach & Gussinklo, 1994).

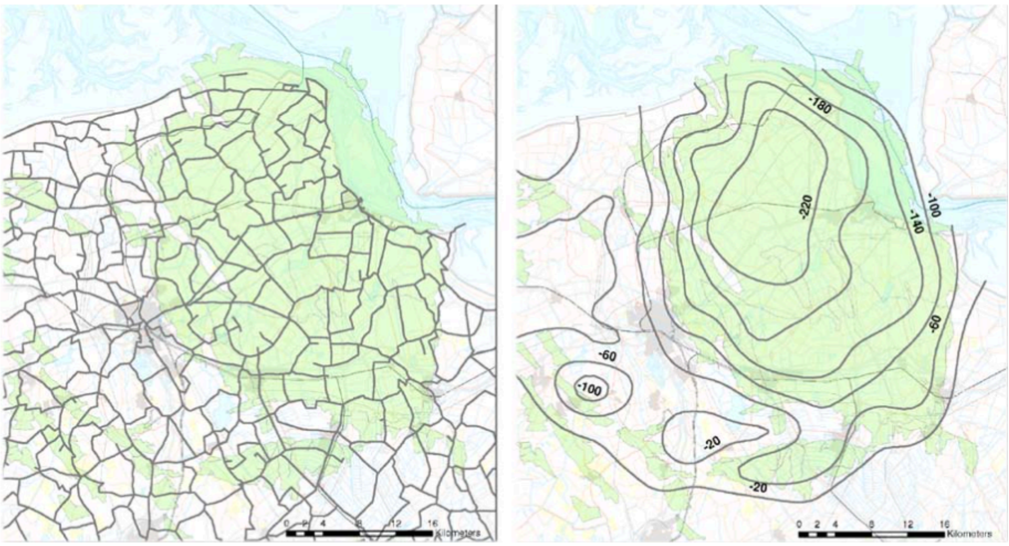

Figure 6.6: Levelling network (left) and subsidence (mm) since start of gas production (right) in the Groningen area in 2003. Gas fields are depicted in green. Copyright (Ketelaar, 2009 Figure 2.6)

Based on the measurement methods previously described, surface subsidence and reservoir compaction have been thoroughly monitored and evaluated in the Groningen field during its production time, and several geomechanical models have been proposed that incorporates both the subsidence and compaction. The observed subsidence rate seems to have changed during the lifetime of the field, apparently proportional to depletion rates. The trend of subsidence with pressure depletion seems to be more linear, but also show tendencies of increasing subsidence rates with increasing pressure depletion. Subsidence was low from production start until 1975, but accelerated after this. This delay in subsidence offset is still not understood properly, although multiple models have been proposed to explain this (van Thienen-Visser & Breunese, 2015). The subsidence bowl related to the production in the

Groningen field is about 40 x 50 km, and the maximum subsidence reached 24.5 cm in 2003 (Dirk Doornhof et al., 2006). Today, the vertical displacement has exceeded 33 cm in the central part of the field, where reservoir thickness and porosity is favourable of compaction (Bourne et al., 2014; van Thienen-Visser & Breunese, 2015). This is also the area where we find the largest fault density and the area of most induced seismicity. The pressure depletion in the Groningen field is fairly uniform, and for most of the field it has accumulated to a pressure drop of about 26MPa, from an initial pore pressure of roughly 35MPa.

There are several factors that may contribute to surface subsidence, including settlement of the construction the benchmark is bolted to, natural compaction of unconsolidated sediments and subsidence do to mining activities or fluid production. In the Groningen field it has been possible to correct the subsidence measurements for shallow compaction since the seventies, when NAM started to monitor sediment compaction between 10 and 400 meters depth using a simple, but sensitive, cable-measurement method. See (D Doornhof, 1992; Dirk Doornhof et al., 2006) or others for further information on subsidence measurement methods in the Groningen area.

7 Numerical model

7.1 Modified Discrete Element Method (MDEM)

A Modified Discrete Element Approach to geomechanical modeling was developed by Alassi (H. T. Alassi, 2008) in order to eliminate the limitations of a discrete element approach while keeping its advantages. The main convenience of this method is that it behaves like a continuum model before failure and like a discontinuum model after failure.

Unlike the original Discrete Element Method (DEM), which works with single elements, this modified approach works with triangular clusters each reaching to three element centres (Figure 7.1). Each cluster can have one of three states, intact cluster which behaves similar to Finite Element Method (FEM), failing cluster which behaves like the conventional DEM, or interface cluster which is used to model faults and predefined cracks. The fundamental relation between the internal forces at the element contacts in DEM and the contact relative displacements are the normal and shear stiffness coefficients, k_n and k_s. For a cluster of three elements, the normal contact forces F_{nm} and the shear forces F_{sm} are related to the relative displacement U in matrix form as:

$$\begin{bmatrix} F_{n1} \\ F_{n2} \\ F_{n3} \\ F_{s1} \\ F_{s2} \\ F_{s3} \end{bmatrix} = \begin{bmatrix} k_{n1} & 0 & 0 & 0 & 0 & 0 \\ 0 & k_{n2} & 0 & 0 & 0 & 0 \\ 0 & 0 & k_{n3} & 0 & 0 & 0 \\ 0 & 0 & 0 & k_{s1} & 0 & 0 \\ 0 & 0 & 0 & 0 & k_{s2} & 0 \\ 0 & 0 & 0 & 0 & 0 & k_{s3} \end{bmatrix} \begin{bmatrix} U_{n1} \\ U_{n2} \\ U_{n3} \\ U_{s1} \\ U_{s2} \\ U_{s3} \end{bmatrix} \tag{7.1}$$

A modification of the DEM is then done by replacing the zeroes in the off-diagonal matrix positions with new stiffness coefficients a_{ij}:

$$\begin{bmatrix} F_{n1} \\ F_{n2} \\ F_{n3} \\ F_{s1} \\ F_{s2} \\ F_{s3} \end{bmatrix} = \begin{bmatrix} k_{n1} & a_{12} & a_{13} & 0 & 0 & 0 \\ a_{21} & k_{n2} & a_{23} & 0 & 0 & 0 \\ a_{31} & a_{32} & k_{n3} & 0 & 0 & 0 \\ 0 & 0 & 0 & k_{s1} & 0 & 0 \\ 0 & 0 & 0 & 0 & k_{s2} & 0 \\ 0 & 0 & 0 & 0 & 0 & k_{s3} \end{bmatrix} \begin{bmatrix} U_{n1} \\ U_{n2} \\ U_{n3} \\ U_{s1} \\ U_{s2} \\ U_{s3} \end{bmatrix} \tag{7.2}$$

The shear unit vector τ_{mi} can be written in term of the normal unit vector I_{mi} as $\tau_{m1}=-I_{m2}$ and $\tau_{m2}=I_{m1}$ at contact m inside the cluster. The stress $\boldsymbol{\sigma} = \begin{bmatrix}\sigma_{xx} & \sigma_{yy} & \sigma_{xy}\end{bmatrix}^T$ may then be written as a function of internal force as follows:

$$\begin{bmatrix} \sigma_{xx} \\ \sigma_{yy} \\ \sigma_{xy} \end{bmatrix}$$

$$= \frac{1}{A} \begin{bmatrix} I_{11}^2 d_1 & I_{21}^2 d_2 & I_{31}^2 d_3 & -I_{12}^2 d_1 & -I_{22}^2 d_2 & -I_{32}^2 d_3 \\ I_{12}^2 d_1 & I_{22}^2 d_2 & I_{32}^2 d_3 & I_{11}^2 d_1 & I_{21}^2 d_2 & I_{31}^2 d_3 \\ I_{11} I_{12} d_1 & I_{21} I_{22} d_2 & I_{31} I_{32} d_3 & -I_{11} I_{12} d_1 & -I_{21} I_{22} d_2 & -I_{33} I_{32} d_3 \end{bmatrix} \begin{bmatrix} F_{n1} \\ F_{n2} \\ F_{n3} \\ F_{s1} \\ F_{s2} \\ F_{s3} \end{bmatrix} \quad (7.3)$$

or in compacted form:

$$\boldsymbol{\sigma} = \frac{1}{A} \mathbf{M}^{\mathbf{T}} \mathbf{F} \quad (7.4)$$

A is the area of the triangle, and can be used instead of volume because we assume that each cluster has a unit thickness.

If we assume that contact m connects two particles p_1 and p_2, then the normal and shear relative displacement U_n^m and U_s^mcan be written as

$$U_n^m = \Delta U_i^m I_i^m \quad (7.5)$$

and

$$U_s^m = \Delta U_i^m - U_n^m I_i^m \quad (7.6)$$

The relative displacement at the contact ΔU_i^m is given as

$$\Delta U_i^m = \varepsilon_{ij} \left(X_j^{p1} - X_j^{p2} \right) \quad (7.7)$$

and the normal unit vector I_i^m is given as

$$I_i^m = \frac{X_i^{p1} - X_i^{p2}}{d_m} \quad (7.8)$$

where d_m is the contact length.

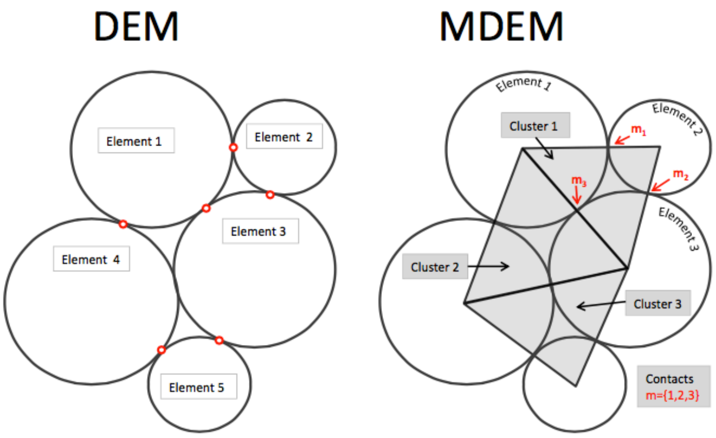

Figure 7.1: Illustration of the DEM and MDEM model schemes. In MDEM the triangular clusters are first looped through to update contact forces before a second loop updates the relative displacements of the nodes. Copyright (Eide, 2014)

This gives us a relation for the strain $\boldsymbol{\varepsilon}$:

$$\mathbf{U} = \mathbf{M}\boldsymbol{\varepsilon} \tag{7.9}$$

where **M** is the unit normal vector matrix for the triangular cluster. We introduce a new input parameter $r=k_{sm}/k_{nm}$, and know that:

$$\boldsymbol{\sigma} = \mathbf{C}\boldsymbol{\varepsilon} \tag{7.10}$$

By using equations (7.2), (7.3), (7.9) and (7.10), we can relate the internal constitutive matrix **K** and the material conventional constitutive matrix **C** to each other:

$$\mathbf{C} = \frac{\mathbf{1}}{\mathrm{A}}\mathbf{M}^{\mathbf{T}}\mathbf{K}\mathbf{M} \tag{7.11}$$

After the internal constitutive matrix has been obtained, the modified approach uses more or less the same solution scheme as regular DEM, but with minor modifications. First the clusters are looped through, and contact forces are updated by using the elements' velocities v_i and the time step *dt* as follows:

$$du_n = ((v_\mathrm{i})^{Element1} - (v_\mathrm{i})^{Element2})\mathrm{I}_\mathrm{i}dt = \Delta v_\mathrm{i}\mathrm{I}_\mathrm{i}dt \tag{7.12}$$

Then forces are applied to each element and the elements' motion is updated using Newton's second law (H. Alassi, Holt, & Landrø, 2010). If the cluster is intact, dU_{nm} are used to calculate the internal contact normal force increments dF_{nm} as in equation (7.2). Normal forces are updated incrementally in this modified method, and the new stress is calculated to check failure. Before failure the shear forces F_{sm} are zero, but if the cluster is failing or of interface type, k_{nm} and k_{sm} are used to calculate the normal and shear forces at each contact and thus shear contact forces will start to build up. The Mohr-Coulomb failure criterion is used to determine shear failure.

The new stiffness coefficient a_{ij} introduced in (7.2) is at this point deleted and contact separation is allowed, and cause the stress to redistribute to surrounding clusters. This can then cause the stresses in these clusters to reach the threshold, resulting in fracture propagation. For the full approach to the MDEM model, the reader is referred to (H. T. Alassi, 2008).

7.2 Mesh Generation

A reservoir is modelled by a triangular mesh in 2D. Since we require a much finer mesh structure near faults and in the reservoir we generate a mesh using DistMesh, a simple mesh generator in MATLAB that describes the mesh shape and nodal spacing by distance functions. The code is based on the physical analogy between a basic mesh and a truss structure. A Delaunay algorithm can triangulate any set of points in the plane, where meshpoints are nodes of the truss, described by x- and y-coordinates, and the edges of the triangles correspond to bars. The external forces in the structure are applied at the boundaries: At every boundary node a reaction force is acting normal to the boundary edge, just large enough to keep the node from moving outside the boundary. Each bar has a force-displacement relationship depending on its current- and its unextended length. The positions of the nodes are found by solving for a static force equilibrium in the structure, where the force vector **F(p)** has horizontal and vertical components at every node:

$$\mathbf{F}(\boldsymbol{p}) = \left[\mathbf{F}_{int,x}(\boldsymbol{p}) \quad \mathbf{F}_{int,y}(\boldsymbol{p})\right] + \left[\mathbf{F}_{ext,x}(\boldsymbol{p}) \quad \mathbf{F}_{ext,y}(\boldsymbol{p})\right] \tag{7.13}$$

where the first column of $\mathbf{F}$ contains the x-components of the forces, and the second column contains the y-components and $\boldsymbol{p}$ gives the position of the nodes. $\mathbf{F}_{\text{int}}$ contains the internal forces from the bars and $\mathbf{F}_{\text{ext}}$ are reactions from the boundaries. $\mathbf{F}(\boldsymbol{p})$ is dependent on the topology of the bars, which is given by the Delaunay triangulation in the algorithm. The Delaunay triangulation maximizes the minimum angle of all the triangles in the triangulation, and thus tend to avoid skinny triangles. The topology is changed by the Delaunay algorithm as the points move, and the force vector is hence not a continuous function of $\boldsymbol{p}$. This discontinuity, together with the external reaction forces at the boundaries, can make it quite hard to solve the system $\mathbf{F}(\boldsymbol{p})=0$. This method solves the system by introducing an artificial time-dependence and approximates it using the forward Euler method: We consider a system of ordinary differential equations for some $\boldsymbol{p}(0)=\boldsymbol{p}_0$,

$$\frac{d\boldsymbol{p}}{dt} = \mathbf{F}(\boldsymbol{p}), \quad \mathrm{t} \geq 0 \tag{7.14}$$

At the discretized time $t_n=n\Delta t$ the approximate solution $\boldsymbol{p}_n \approx \boldsymbol{p}(t_n)$ is updated by

$$\boldsymbol{p}_{n+1} = \boldsymbol{p}_n + \Delta\mathrm{t}\mathbf{F}(\boldsymbol{p}_n) \tag{7.15}$$

The mesh information is stored in three variables “**p**”, “**t**” and “**edge**”:

- **p**: N×2 matrix containing the coordinates of the N mesh nodes.
- **t**: N_e×3 matrix containing the indices of the three nodes spanning each of the N_e elements of the mesh.
- **edge**: N_t×2 matrix containing the indices of the two nodes spanning each of the N_t boundary bars on the edge of the domain

For a full description of the algorithm and the complete MATLAB code the reader is referred to (Persson & Strang, 2004).

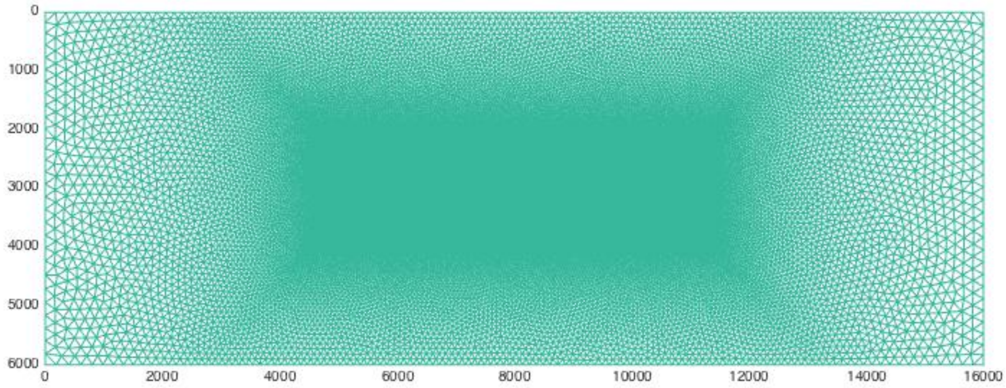

Figure 7.2: Example of a 2D triangulated mesh generated by the MATLAB script.

With the mesh generated, we can then manipulate the stored information with a simple MATLAB script so that it complies with the desired input file for the MDEM code. The generated code can be found in Appendix: A.

7.2.1 Model Geometry

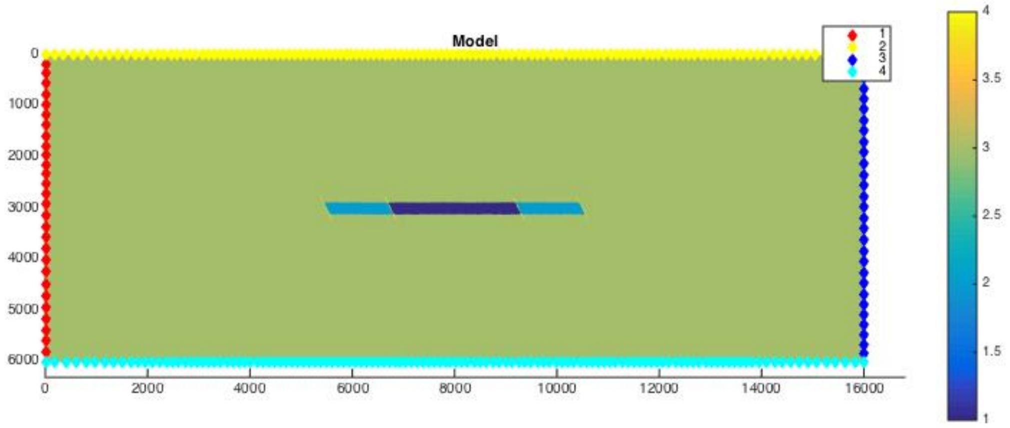

Figure 7.3: Example model with 3 reservoir compartments, seperated by faults.

Figure 7.3 shows a basic model used in the MDEM simulation. It illustrates a reservoir at 3000 m depth with a thickness of 240 m and a horizontal extent of 5000 m. The reservoir is bounded by faults on both ends and the three reservoir compartments are also separated by faults. All of these faults stretch from 120 m below the reservoir to 120 m into the overburden. The central compartment is assigned a different domain than the adjacent compartments and may thus be assigned different rock parameters and pressure conditions than the other two compartments. An extensive sideburden is established to prevent interference between the induced stresses from the boundaries and the reservoir.

7.2.2 Model Parameters

As the models used in the simulations are extreme simplifications of the actual reservoir geometry in the Groningen field, little effort has been made to mirror the exact rock properties measured in the field. The goal of this thesis is to investigate the possible effect of different properties and mechanisms on induced seismicity in a producing gas field and the rock masses are therefore assigned generally reasonable values used in similar simulations. This implies that the values are selected to promote a smooth-running model, and should not be regarded as anything more. Table 7.1 gives an overview of the values of reservoir rock properties used in the basic model. The overburden is assigned elastic properties representing an impermeable weak shale. The faults have been defined as weak zones in the rock mass, and the clusters in these zones are still intact at the start of production in order to simulate an initially locked fault system. The initial pore pressure in the model is calculated straightforward from the weight of the water column and the boundaries are fixed on all sides except the top.

	Reservoir rock
Bulk density [kg/m3]	2700
Bulk modulus [GPa]	6
Shear modulus [GPa]	1
Tensile strength [MPa]	1.6
Shear strength [MPa]	5.7

Table 7.1: Rock properties of the reservoir rock used in the model.

8 Results

An extensive number of simulations have been done with a range of mesh sizes in order to adjust the model and rock parameters in order to obtain a smooth-running model and a stable solution. Three different models have been included in this thesis: Model 1 (Figure 8.1) represents a reservoir where the reservoir itself and its three reservoir compartments are bound by parallel faults. Model 2 (Figure 8.7) and Model 3 (Figure 8.13) have a horst-graben type geometry, where Model 2 has uniform thickness and Model 3 illustrates the central compartment as a graben structure that later has been upthrown due to reversal of the stress regime. All three models have reservoirs centred at depth of 3000 m, and the initial thicknesses are 240 m except for the central compartment in Model 3, which has a thickness of 280 m. The reservoir in Model 1 has a horizontal extent of 5000 m, while the reservoirs in Model 2 and Model 3 both have an extent of 4000 m. Faults stretch 120 m into the underburden and overburden, except from the reservoir bounding faults in Model 2 and Model 3 which stretch 200 m above and below the reservoir.

The meshes used in the final simulations are defined by the following properties:

	Model 1	Model 2	Model 3
Initial bar length [m]	10	10	10
N_{Nodes}	56.903	43.166	43.094
$N_{Elements}$	113.494	86.084	85.940

Table 8.1: Mesh properties of the meshes used in the simulations.

Each model has been depleted twice, first with a homogeneous depletion rate in all reservoir compartments and then with a 30% decrease in depletion rate in the two outer compartments. The reservoir is depleted in four steps, and for the faults the mean depletion rate of the two reservoir domains is assumed.

Each simulation is presented by figures showing the stress state, pressure distribution, failed elements and induced strains. Note that the scale of the colour bar changes, and that strains are assigned a logarithmic scale. For each simulation the surface subsidence caused by the pressure depletion is plotted (Figures 8.6, 8.12 and 8.18). An overview of the results is presented here, followed by an analysis and discussion of these in the next section. All plots have been generated using the MDEM code in MatLab and editing has been done by the default MatLab Plot Editor.

MODEL 1

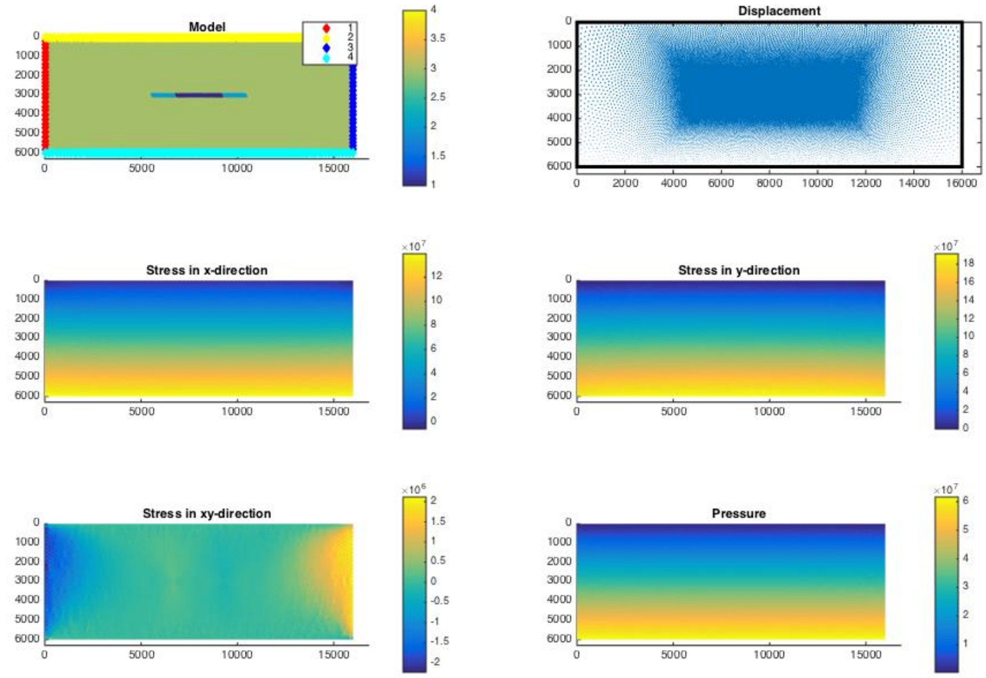

Figure 8.1: Initial state of Model 1, used in Simulation 1.1 and 1.2

Simulation 1.1

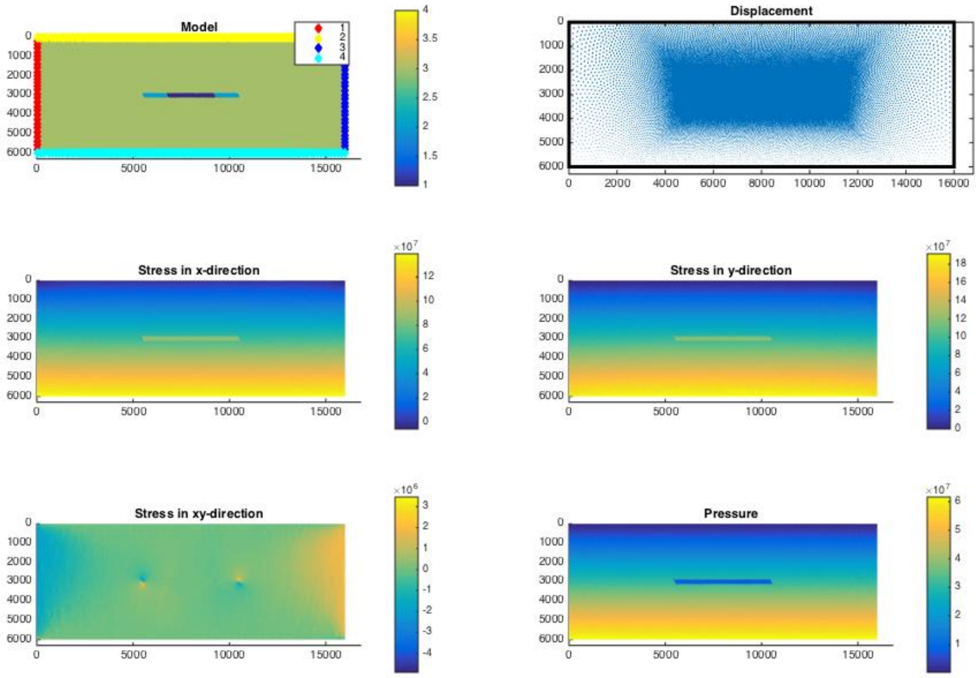

Model

Displacement

Stress in x-direction

Stress in y-direction

Stress in xy-direction

Pressure

Figure 8.2: Reservoir depleted to 8MPa in all reservoir compartments. No fault reactivation, but note shear stresses on reservoir edges.

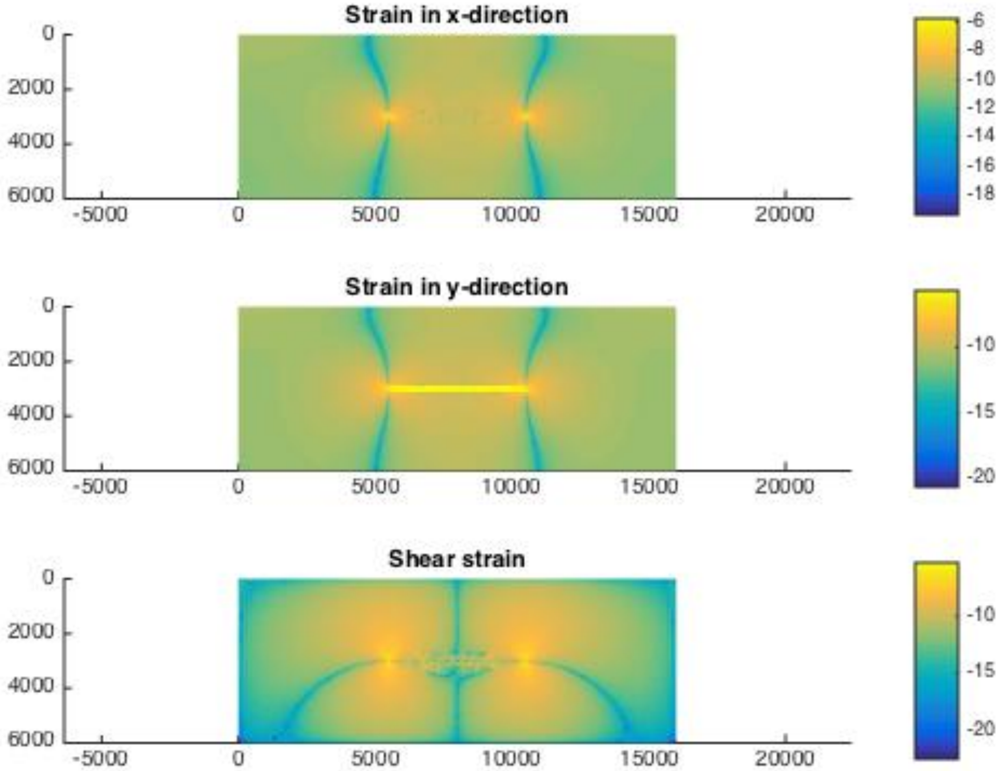

Figure 8.3: Subsurface strains due to reservoir depletion. Note extensive compaction inside reservoir and shar strains on the edges of the reservoir.

Simulation 1.2

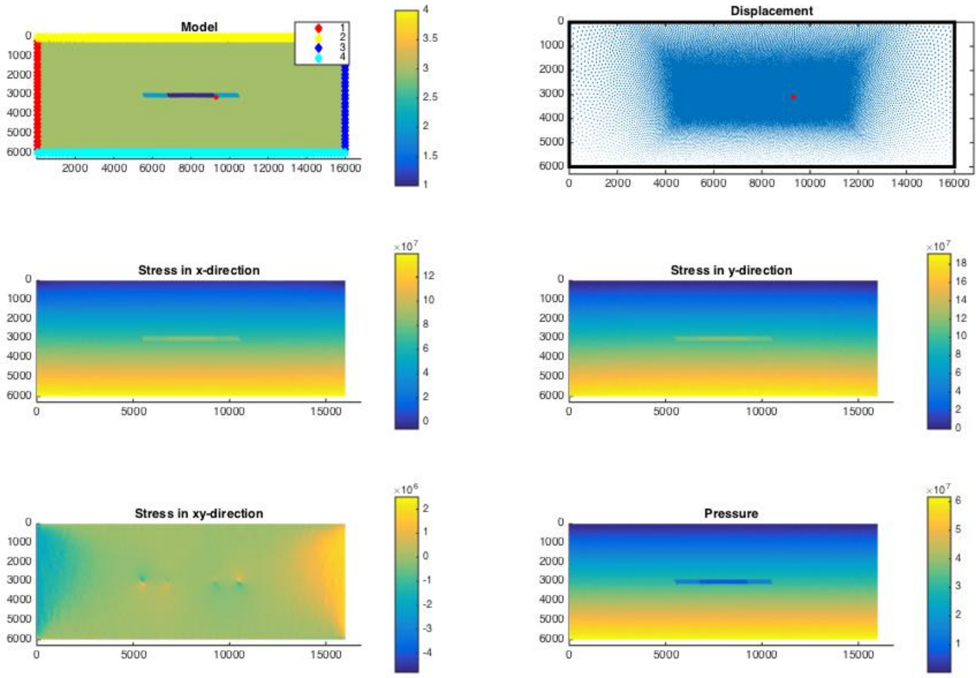

Figure 8.4: Simulation with depletion target 8MPa in centre reservoir and ~15MPa in adjacent compartments. Note fault reactivation in the lower part of the reservoir.

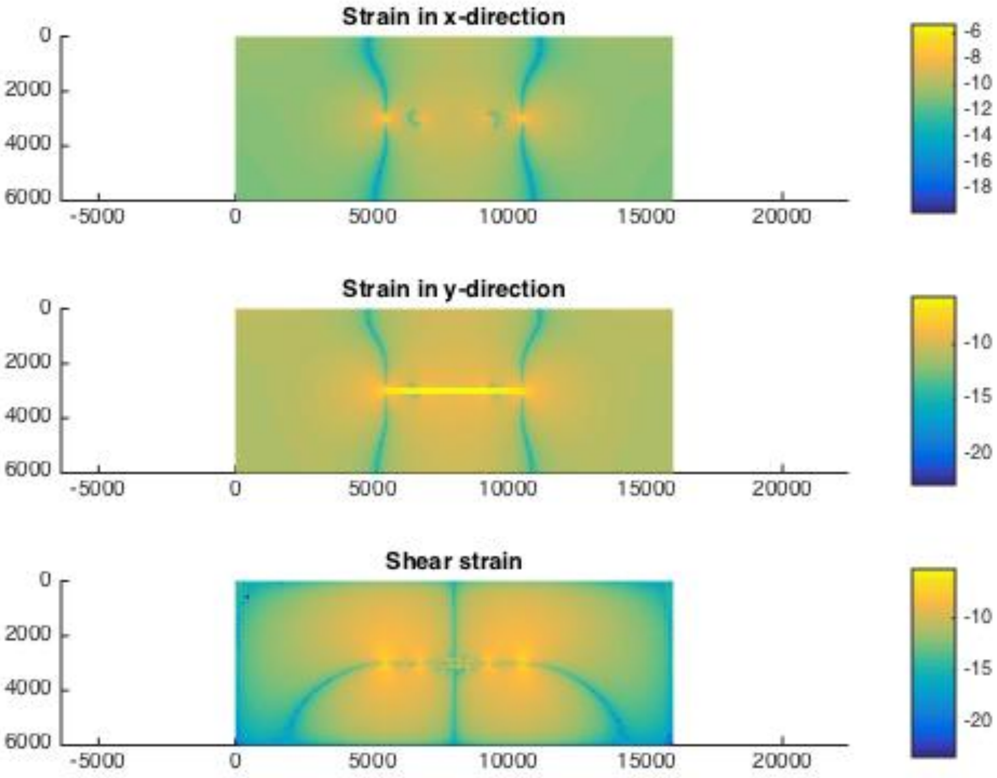

Figure 8.5: Subsurface strains due to reservoir depletion.

Subsidence in Model 1

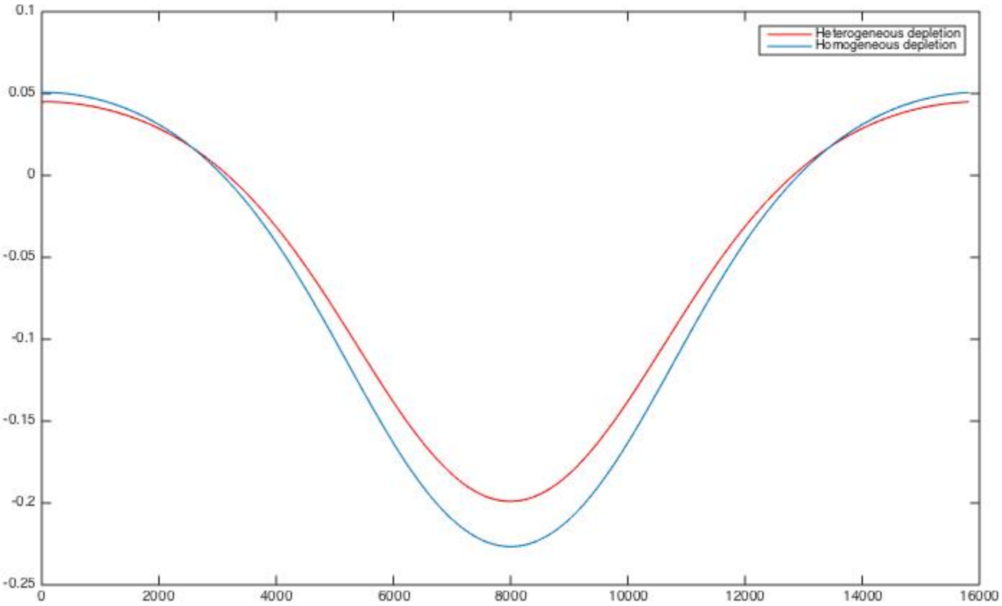

Figure 8.6: Subsidence due to depletion in Simulation 1.1 and 1.2

MODEL 2

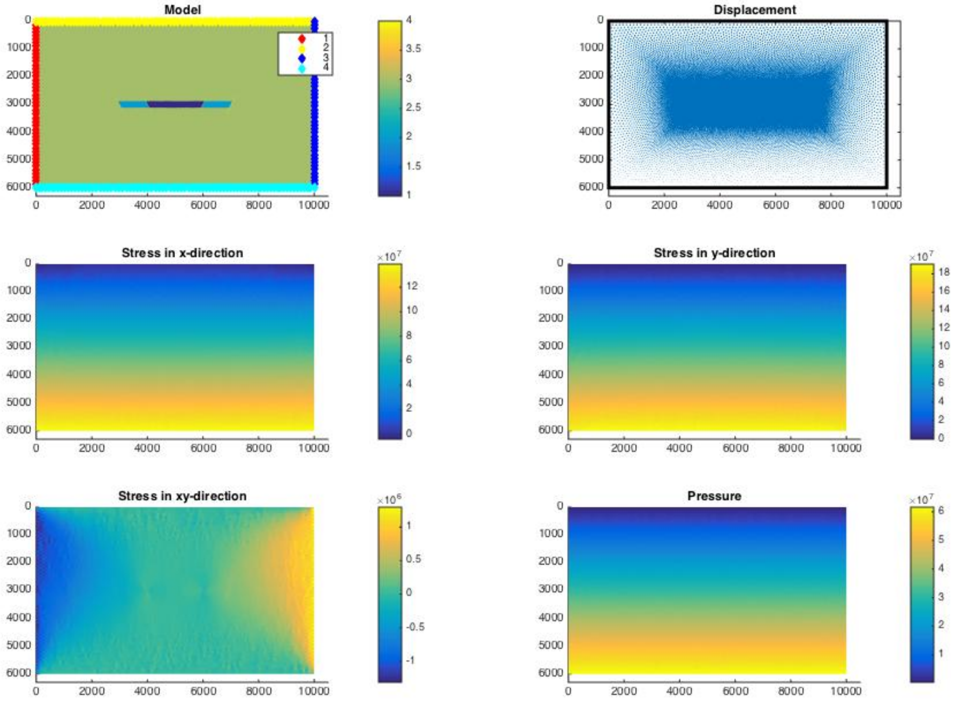

Figure 8.7: Model 2, used in Simulation 2.1 and 2.2

Simulation 2.1

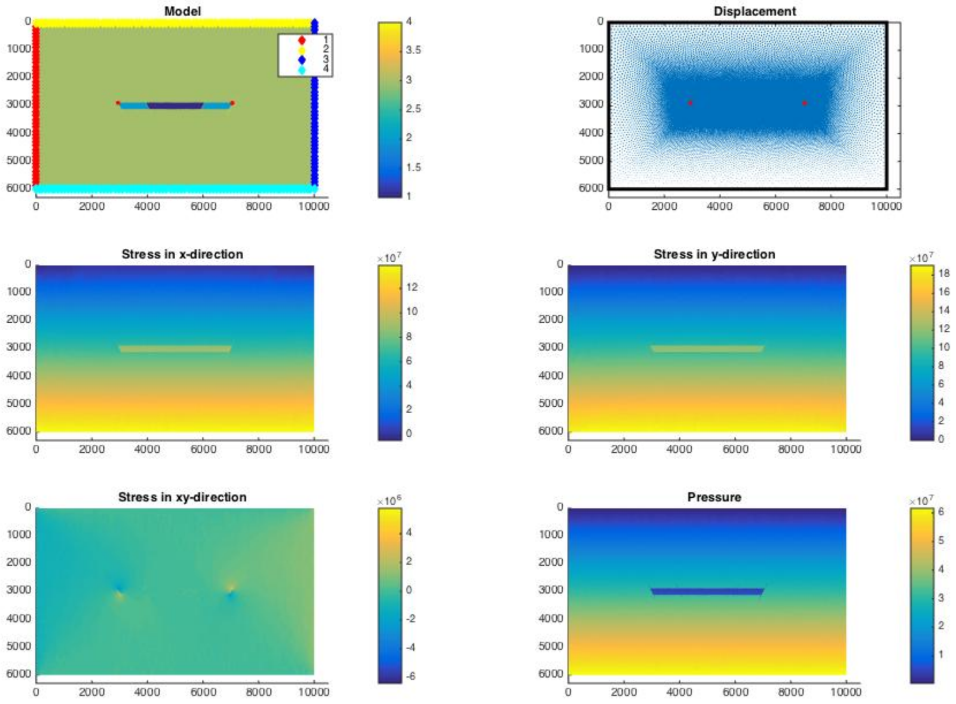

Figure 8.8: Reservoir depleted to 5MPa in all reservoir compartments. Note fault reactivation on the upper corners of the reservoir.

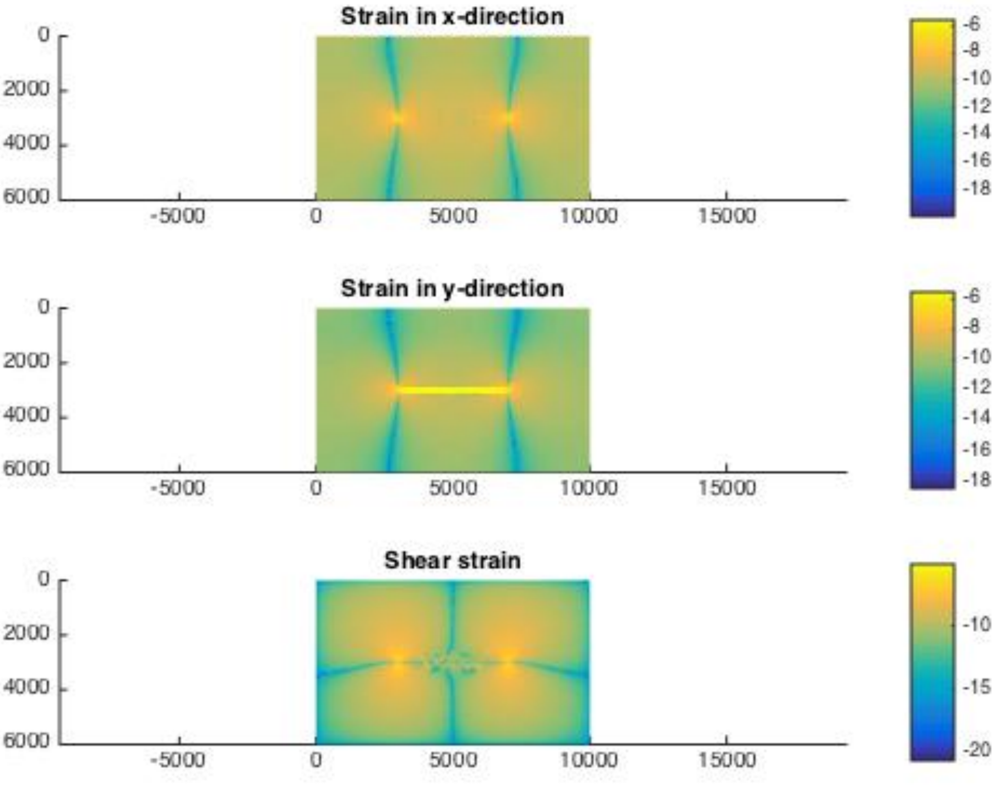

Figure 8.9: Subsurface strains due to reservoir depletion.

Simulation 2.2

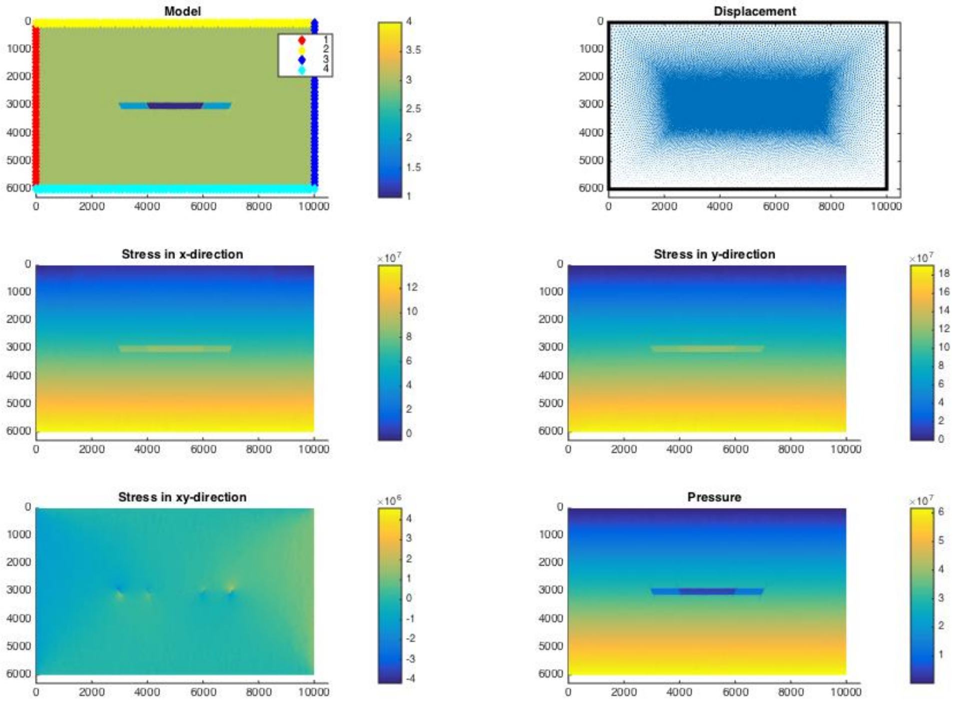

Figure 8.10: Simulation with depletion target 5MPa in centre reservoir and ~13MPa in adjacent compartments. No fault reactivation.

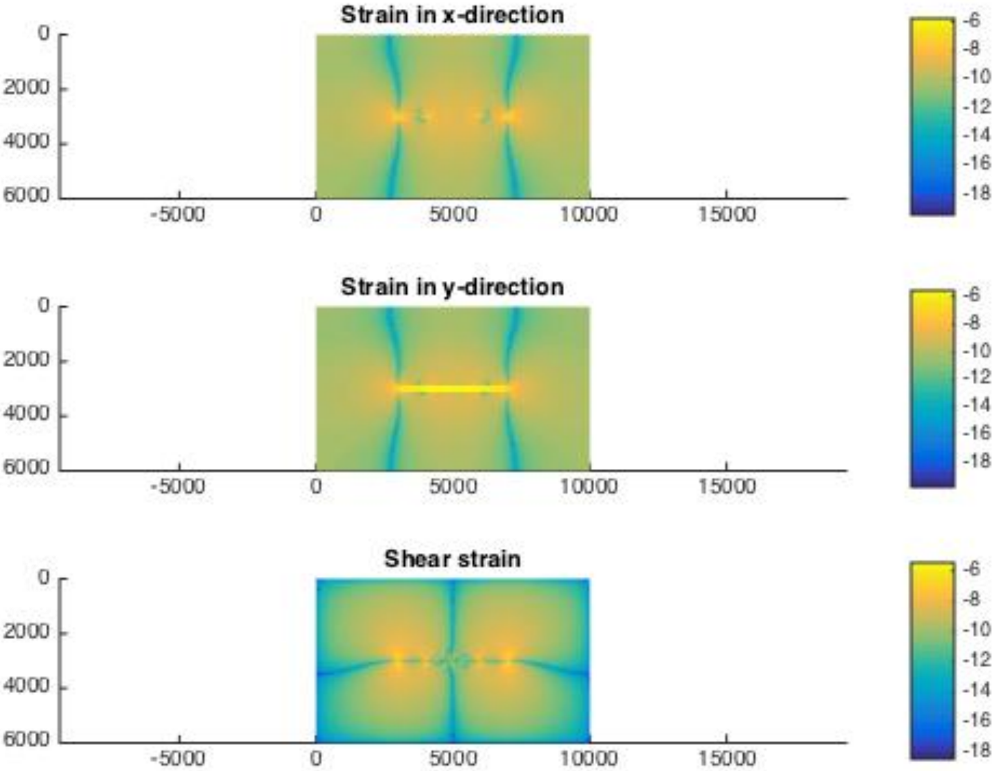

Figure 8.11: Subsurface strains due to reservoir depletion.

Subsidence in Model 2

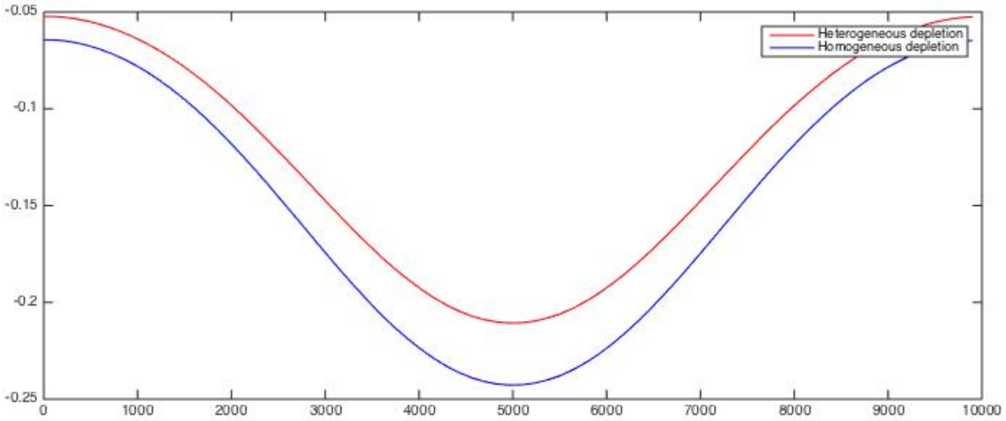

Figure 8.12: Subsidence due to depletion in Simulation 2.1 and 2.2

MODEL 3

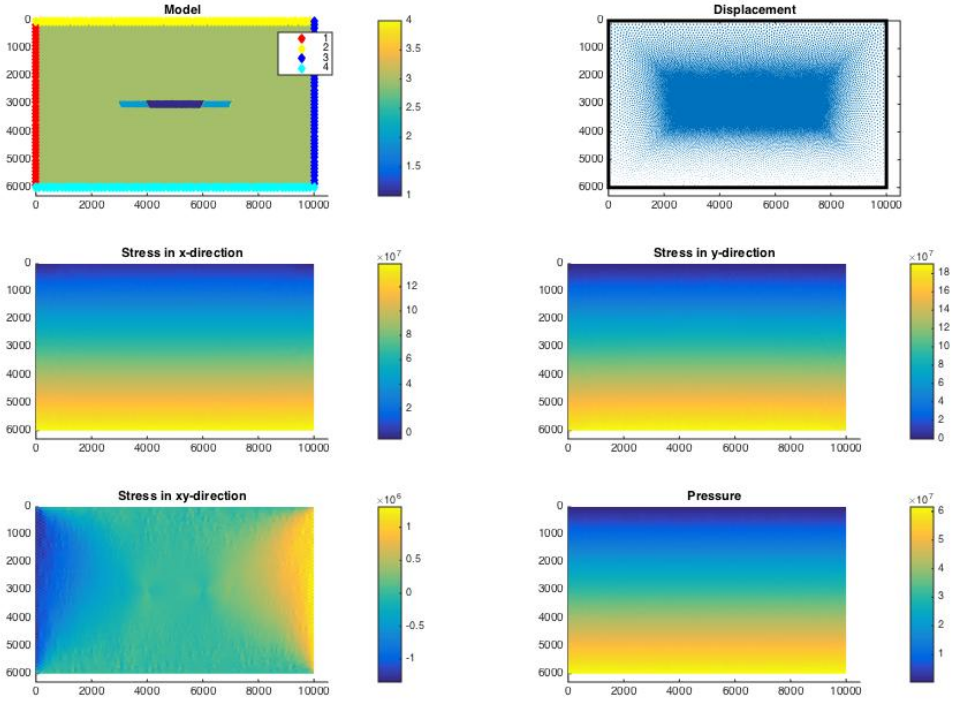

Figure 8.13: Model 3, used in Simulation 3.1 and 3.2

Simulation 3.1

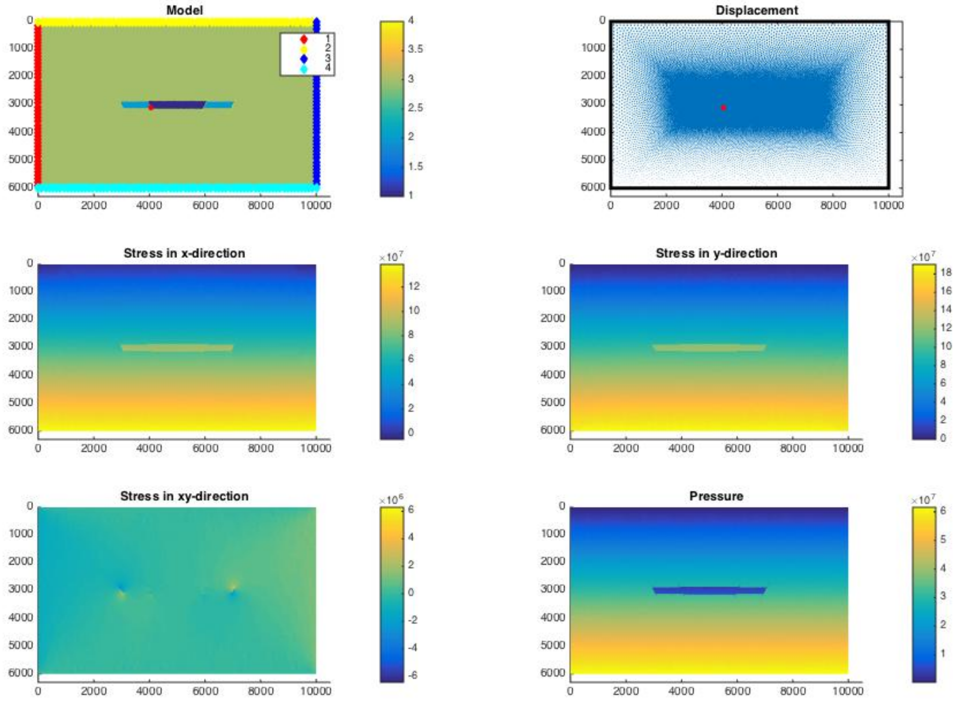

Figure 8.14: Reservoir depleted to 5MPa in all reservoir compartments. Fault reactivation inside reservoir.

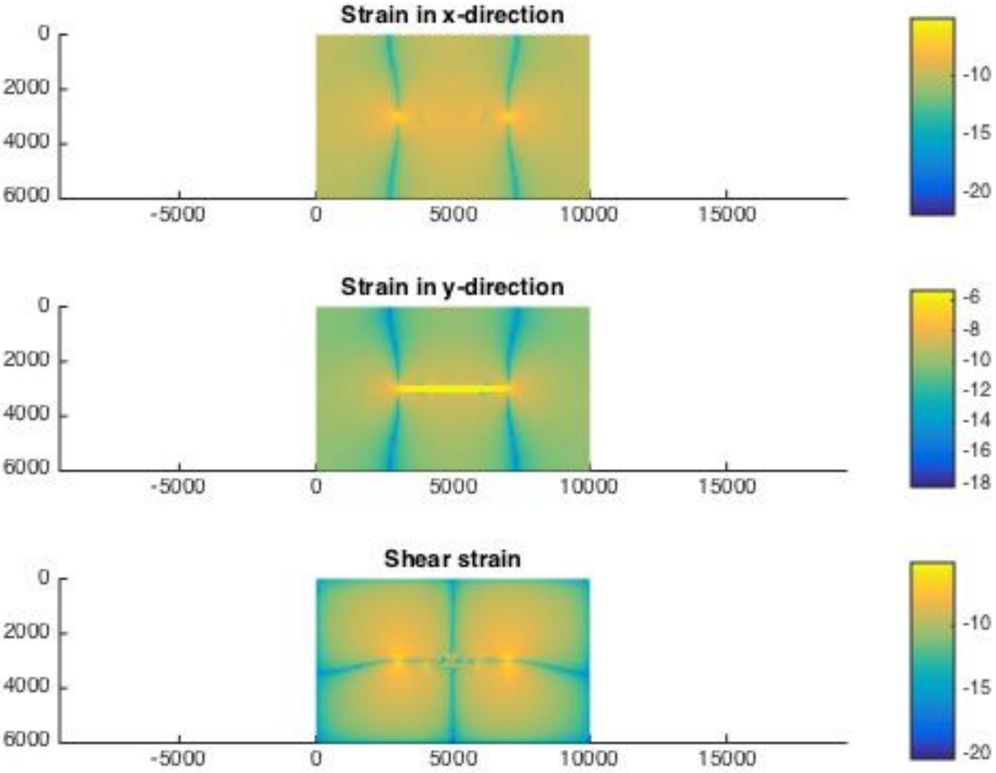

Figure 8.15: Subsurface strains due to reservoir depletion.

Simulation 3.2

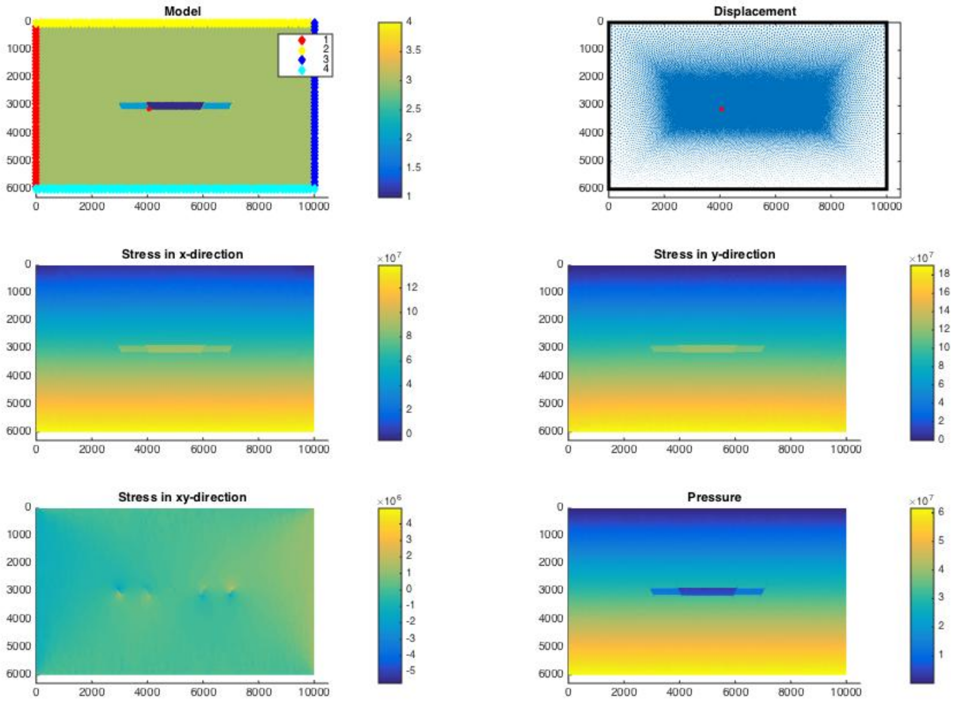

Figure 8.16: Simulation with depletion target 5MPa in centre reservoir and ~13MPa in adjacent compartments. Fault reactivation inside reservoir.

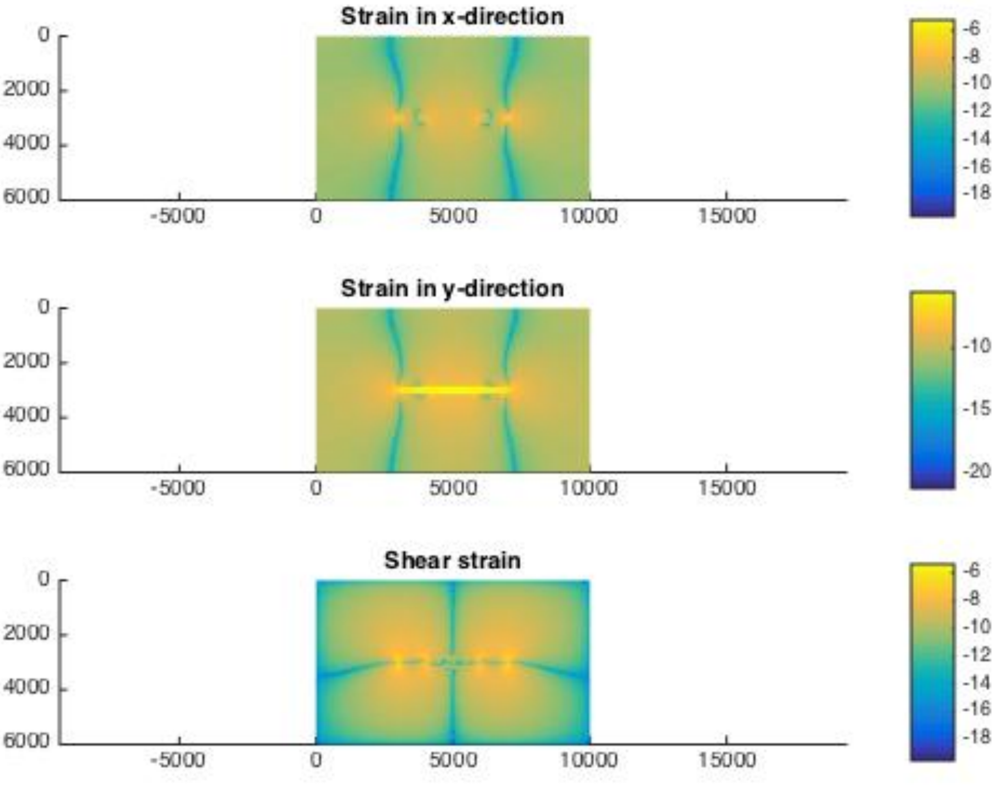

Figure 8.17: Subsurface strains due to reservoir depletion.

Subsidence in Model 3

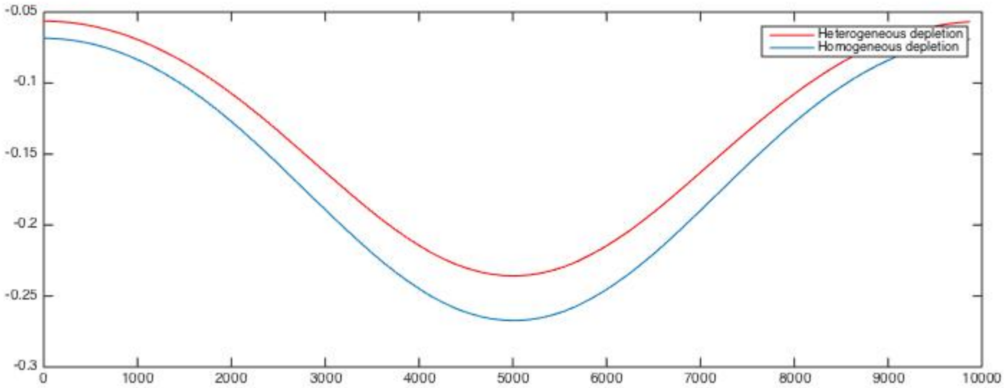

Figure 8.18: Subsidence due to depletion in Simulation 3.1 and 3.2

9 Discussion and Further Work

From the depletion plots it is evident that depletion has a significant impact on reactivation of faults in a reservoir. Although the stress regime and rock parameters in the model do not mirror the actual Groningen reservoir, it successfully addresses the significance of the key parameters of fault reactivation in vicinity of a producing reservoir.

As previously stated, the 2D model used in the simulations must be regarded as a very simplified representation of the Groningen Field. In the model, all the rock mass surrounding the reservoir has been assigned the same rock properties representative of weak shale. In reality, the top seal in the South Permian Basin consist of the Zechstein evaporites, and ideally a viscoelastic caprock should thus have been applied to the model. It can however be argued that the effects introduced by the presence of salt can be neglected in our model since the Ten Boer claystone may be regarded as a regional seal in the area. For a thorough discussion of the geomechanical effects introduced by viscoelastic caprocks, the reader is referred to (Orlic and Wassing 2012).

The fault geometry in the Groningen Field is complex, and simplifications had to be made in the 2D model. Faults in our model are restricted to the area in, and in the vicinity of, the reservoir due to increasing element sizes outside the reservoir. Several fault geometries were modelled, including parallel faults and a horst-graben type fault system as presented, and it appears that the fault orientation is of great significance in our 2D case. The strengths of the faults are unknown, and especially the shear strength of the faults is assumed to be too low in the model. This will promote fracture propagation. Another issue concerning the modelled faults is regarding the pressure evolution during depletion. In the simulations the depletion rate in the faults is assumed to be the mean value of depleting reservoir zones. This does not mirror the real case, and the implementation of a flow simulator would be beneficial.

The stress regime initiated in the model is a poor representation of the actual field case. The model calculates the vertical and horizontal stresses from gravity, this implies that stresses increase with depth dependent on the weight of the overburden and pore fluid. In this model, brine is set as the pore fluid. The stress is applied on the top of the domain, and because the generated mesh is unstructured this introduces some shear stress on the side boundaries due to differences in element size. This could be avoided by setting a structured grid at the boundaries, but the designed mesh generator does not support structured grid geometry. Thus the structured grid would have to be set manually node for node, and because this is very tedious work the issue has been avoided by assigning the model an extensive side burden. We have the possibility to initiate stresses that are similar to the stresses in the Groningen reservoir, but this would neglect the vertical stress variations and is therefore not prioritized.

Simulation 1.1 did not cause any element failure, but significant shear stress and strains could be observed on the faults at the reservoir edges, especially around the corners of the reservoir. It is believed that the corners were very close to failure, and if the depletion had continued shear failure would occur as is seen in Simulation 2.1. In Simulation 1.2 the depletion rate in the outer reservoir compartments was reduced by 30%, thus decreasing the stresses on the edge of the reservoir. However, due to differential depletion in the reservoir compartments shear failure occurred on the fault separating two of the compartments. This was not observed in Simulation 2.2 despite the lower depletion target. This may be due to different fault geometry in the two models.

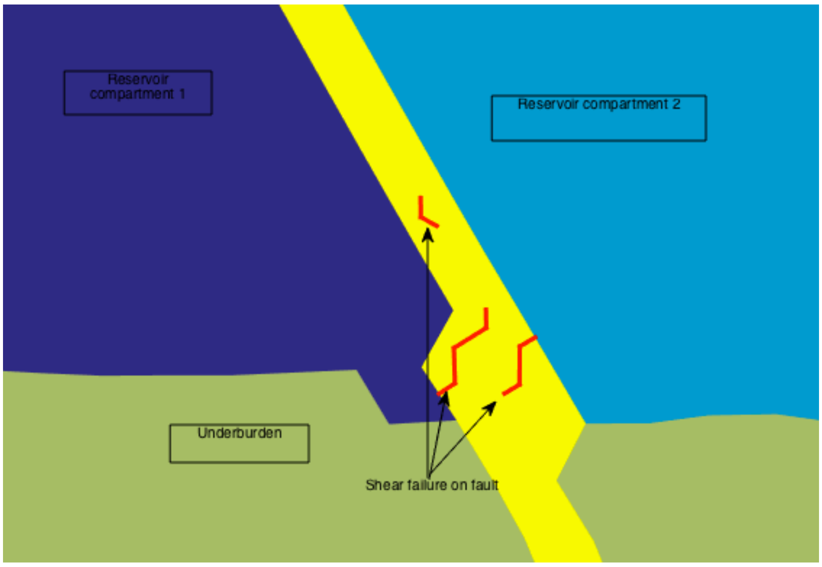

Figure 9.1: Close-up from Figure 8.6 showing shear failure on the fault seperating two reservoir compartments.

Both Simulation 3.1 and Simulation 3.2 resulted in shear failure on the fault separating the central reservoir compartment and an outer compartment. It appears that a thicker central compartment encourages fault reactivation in the reservoir.

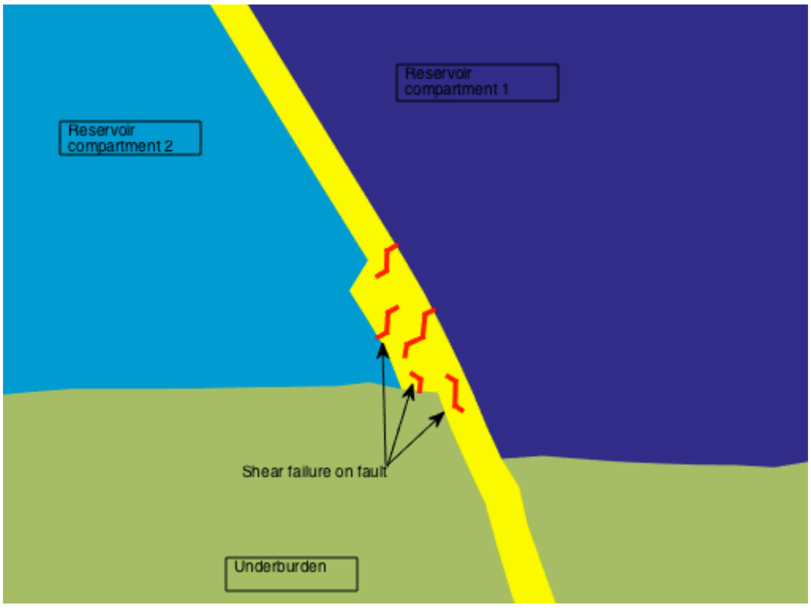

Figure 9.2: Close-up from Figure 8.14. Fault reactivation between two reservoir compartments.

The observed element failure in the simulations may not seem very consequential, but given that the initial bar length of the elements are 10 m, the fault area undergoing slip may be significant depending on the geometry of the fault zone. The sizes of the failure events are believed to be reasonable, and the MDEM code appears to produce reliable results. This is supported by the observation that for simulations where the strength of the faults have been too low, causing all fault elements to fail, a logarithmic power-law distribution have been found when plotting estimated released energy with frequency of the events (Figure 9.3).

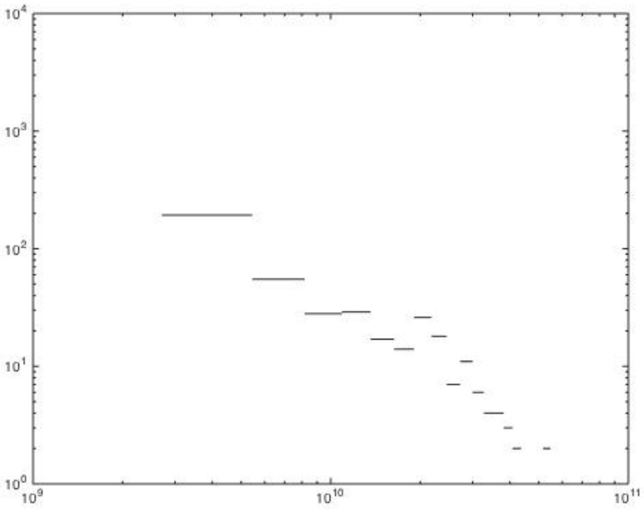

Figure 9.3: Observed power-law distribution caused by failure of all fault elements in an unsuccessful simulation.

The subsidence plots appear reasonable, and fits well with the analytical solution described in Section 2.1.2. It should be mentioned that the apparent uplift on the sides of the subsidence bowl in Simulation 1.1 and Simulation 1.2 is caused by the initial settlement of the model and should most likely be close to zero. In Figure 9.3 all the subsidence plots from Model 2 and Model 3 are presented. It is evident that pressure decrease and thicknesses of the depleted zones are critical indicators of surface subsidence.

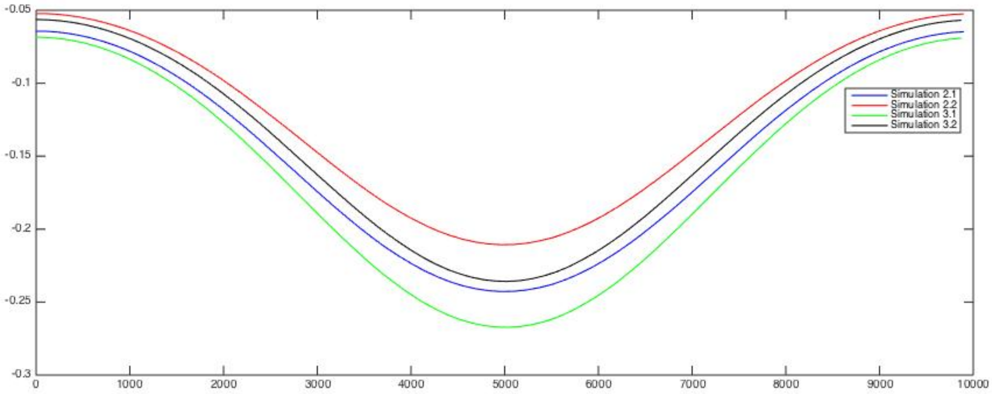

Figure 9.4: Subsidence in Model 2 and Model 3

Despite the clear limitations of the model, mainly associated with the model geometry and simplifications, it is assumed that it provides a robust and time-efficient tool for simulating the geomechanical changes induced by pore pressure depletion in a gas reservoir. The simplicity of the model may also be one of its strengths, as this allows us to address and investigate the significance of a small number of parameters.

9.1 Proposed Further Work

The focus of this thesis is on identifying factors contributing to induced seismicity in vicinity of oil and gas fields. Some of the key parameters have been addressed in a numerical study. For further studies, it is proposed to do numerical studies on the other factors discussed in Chapter 3, as well as improve the MDEM code used for the simulations. It will be an advantage for the user to have access to the source code when working with MDEM. The MDEM code can be coupled to a flow simulator, and it is believed that this would improve the representation of a depleting reservoir. Also secondary effects of e.g. thermal and chemical effects could be relevant in the future. For better understanding of induced seismicity, the following themes are proposed:

- Continue the work of this thesis: Continue the work of this thesis by running more simulations with different geometries and rock properties.
- Mirror the in-situ stress regime in the Groningen Field: Improve the MDEM code used in the thesis by including stress zones and possibly also to include heterogeneity in the rock properties.
- Include a viscoelastic caprock in the model.
- Tie the model to a flow simulator: By coupling the model to a flow simulator the effects of a hydrodynamic front could be investigated and the simulations would be more realistic. Fluid injection could be simulated, and thermal effects could also be added to address the significance of thermal stress caused by the injected fluid.
- Address the effect of mass transfer: Through coupling with a flow simulator the significance of mass transfer could be investigated.
- 3D model: The MDEM code could be developed to work in three dimensions. This would be beneficial for investigating how the reservoir and fault geometries influence the induced seismicity.

10 Conclusion

Reservoir compaction and associated surface subsidence and induced seismicity are growing socio-economic concerns in many regions in vicinity of oil and gas fields, and a better understanding of geomechanical changes in the subsurface due to hydrocarbon exploitation is a necessity in the petroleum industry. Many studies have been executed over the past decades in order to tie reservoir compaction to subsidence and to identify the underlying causes of induced seismicity. However, especially for the latter, the conclusions have often been disputed and contradicting. This thesis has addressed induced seismicity and subsidence with special attention to the Groningen Field. A numerical approach has been carried out to simulate a depleting gas reservoir using a Modified Discrete Element Method. Several simulations were conducted to study the effects of depletion-induced stresses in a fault compartmentalized reservoir. Fault reactivation was observed between the reservoir compartments due to differential depletion and thickness variations. Reactivation of reservoir bounding faults was also observed after significant pore pressure reduction. The simple model proved to be a robust and effective tool for simulating geomechanical changes and additional improvements are proposed for potential further work.

References

Addis, M., Hanssen, T., Yassir, N., Willoughby, D., & Enever, J. (1998). A comparison of leak-off test and extended leak-off test data for stress estimation. *SPE/ISRM Rock Mechanics in Petroleum Engineering*.

Alassi, H., Holt, R., & Landrø, M. (2010). Relating 4D seismics to reservoir geomechanical changes using a discrete element approach. *Geophysical Prospecting, 58*(4), 657-668.

Alassi, H. T. (2008). *Modeling reservoir geomechanics using discrete element method: Application to reservoir monitoring.* PHD Thesis, Norwegian University of Science and Technology (NTNU).

Bak, P. (1997). *How nature works*: Oxford university press Oxford.

Bak, P., & Tang, C. (1989). Earthquakes as a self-organized critical phenomenon. *Journal of Geophysical Research: Solid Earth (1978–2012), 94*(B11), 15635-15637.

Bak, P., Tang, C., & Wiesenfeld, K. (1987). Self-organized criticality: An explanation of the 1/f noise. *Physical review letters, 59*(4), 381.

Bjørlykke, K. (2010). *Petroleum geoscience: From sedimentary environments to rock physics*: Springer Science & Business Media.

Bourne, S., Oates, S., Elk, J., & Doornhof, D. (2014). A seismological model for earthquakes induced by fluid extraction from a subsurface reservoir. *Journal of Geophysical Research: Solid Earth, 119*(12), 8991-9015.

Brouwer, G. (1972). The Rotliegend in the Netherlands. *Rotliegend, Essays on European Lower Permian, ed, by H. Falke, Brill, Leiden*, 34-42.

Davis, S. D., & Pennington, W. D. (1989). Induced seismic deformation in the Cogdell oil field of west Texas. *Bulletin of the Seismological Society of America, 79*(5), 1477-1495.

Day, R. (2012). *Geotechnical Earthquake Engineering*: McGraw Hill Professional.

Doornenbal, H., & Stevenson, A. (2010). *Petroleum geological atlas of the Southern Permian Basin area*: EAGE.

Doornhof, D. (1992). SURFACE SUBSIDENCE IN THE NETHERLANDS-THE GRONINGEN GAS-FIELD. *Geologie en Mijnbouw, 71*(2), 119-130.

Doornhof, D., Kristiansen, T. G., Nagel, N. B., Pattillo, P. D., & Sayers, C. (2006). Compaction and subsidence. *Oilfield Review, 18*(3), 50-68.

Eide, V. V. (2014). Numerical Simulation of Extended Leak-Off Tests.

Fielding, E. J., Blom, R. G., & Goldstein, R. M. (1998). Rapid subsidence over oil fields measured by SAR interferometry. *Geophysical Research Letters, 25*, 3215-3218.

Fjær, E., Holt, R. M., Raaen, A., Risnes, R., & Horsrud, P. (2008). *Petroleum related rock mechanics* (Vol. 53): Elsevier.

Frikken, H. (1999). *Reservoir-geological aspects of productivity and connectivity of gas reservoirs in the Netherlands.* Ph. D. thesis Delft University of Technology: 92 pp.

Garcia, A., & MacBeth, C. (2013). An estimation method for effective stress changes in a reservoir from 4D seismics data. *Geophysical Prospecting, 61*(4), 803-816.

Geertsma, J. (1966). *Problems of rock mechanics in petroleum production engineering.* Paper presented at the 1st ISRM Congress.

Geertsma, J. (1973). Land subsidence above compacting oil and gas reservoirs. *Journal of Petroleum Technology, 25*(6), 734-744.

Geluk, M. C. (2005). Stratigraphy and tectonics of Permo-Triassic basins in the Netherlands and surrounding areas. *Utrecht University*.

Grant, L. B., & Lettis, W. R. (2002). Introduction to the special issue on paleoseismology of the San Andreas fault system. *Bulletin of the Seismological Society of America, 92*(7), 2551-2554.

Grasso, J.-R. (1992). Mechanics of seismic instabilities induced by the recovery of hydrocarbons. *Pure and Applied Geophysics, 139*(3-4), 507-534.

Grasso, J. R., & Sornette, D. (1998). Testing self-organized criticality by induced seismicity. *Journal of Geophysical Research: Solid Earth (1978–2012), 103*(B12), 29965-29987.

Hazzard, J., & Young, R. (2004). Dynamic modelling of induced seismicity. *International Journal of Rock Mechanics and Mining Sciences, 41*(8), 1365-1376.

Hettema, M., Schutjens, P., Verboom, B., & Gussinklo, H. (2000). Production-induced compaction of a sandstone reservoir: the strong influence of stress path. *SPE Reservoir Evaluation & Engineering, 3*(04), 342-347.

Hooper, J. (2014). L'Aquila earthquake scientists win appeal, The Guardian November 10th 2014.

Hough, S. E. (2007). *Richter's Scale: Measure of an Earthquake, Measure of a Man*: Princeton University Press.

Ilinski, A., & Krasnova, M. (2010). Location of microearthquakes sources at passive seismic monitoring of hydraulic fracturing. *Seismic Instruments, 46*(3), 213-222.

Izadi, G., & Elsworth, D. (2014). Reservoir stimulation and induced seismicity: Roles of fluid pressure and thermal transients on reactivated fractured networks. *Geothermics, 51*, 368-379.

Ketelaar, V. (2009). Subsidence Due to Hydrocarbon Production in the Netherlands. *Satellite Radar Interferometry: Subsidence Monitoring Techniques*, 7-26.

Landrø, M. (2010). Anvendt geofysikk.

Malamud, B. D., & Turcotte, D. L. (1999). Self-organized criticality applied to natural hazards. *Natural Hazards, 20*(2-3), 93-116.

Maury, V., Grasso, J.-R., & Wittlinger, G. (1992). Monitoring of subsidence and induced seismicity in the Lacq gas field (France): the consequences on gas production and field operation. *Engineering Geology, 32*(3), 123-135.

Maxwell, S. C., & Urbancic, T. I. (2001). The role of passive microseismic monitoring in the instrumented oil field. *The Leading Edge, 20*(6), 636-639.

Mayuga, M., & Allen, D. (1969). *Subsidence in the Wilmington Oil Field, Long Beach, California, USA.* Paper presented at the Proceedings of Tokyo Symposium on Land Subsidence.

McGarr, A. (1991). On a possible connection between three major earthquakes in California and oil production. *Bulletin of the Seismological Society of America, 81*(3), 948-970.

McLaskey, G. C., & Glaser, S. D. (2011). Micromechanics of asperity rupture during laboratory stick slip experiments. *Geophysical Research Letters, 38*(12).

Mes, M. J., & Landau, H. (1995). *Ekofisk automatic GPS subsidence measurements.* Paper presented at the OCEANS'95. MTS/IEEE. Challenges of Our Changing Global Environment. Conference Proceedings.

Mobach, E., & Gussinklo, H. (1994). *In-situ reservoir compaction monitoring in the Groningen field.* Paper presented at the Rock Mechanics in Petroleum Engineering.

Nagel, N. (2001). Compaction and subsidence issues within the petroleum industry: From Wilmington to Ekofisk and beyond. *Physics and Chemistry of the Earth, Part A: Solid Earth and Geodesy, 26*(1), 3-14.

NPD, F. p. (2014). Faktaside Ekofisk: http://factpages.npd.no/factpages/Default.aspx?culture=nb-no&nav1=field&nav2=PageView%7CAll&nav3=2053062.

Ottemöller, L., Nielsen, H., Atakan, K., Braunmiller, J., & Havskov, J. (2005). The 7 May 2001 induced seismic event in the Ekofisk oil field, North Sea. *Journal of Geophysical Research: Solid Earth (1978–2012), 110*(B10).

Pennington, W. D., Davis, S. D., Carlson, S. M., DuPree, J., & Ewing, T. E. (1986). The evolution of seismic barriers and asperities caused by the depressuring of fault planes in oil and gas fields of South Texas. *Bulletin of the Seismological Society of America, 76*(4), 939-948.

Perrodon, A. (1983). *Dynamics of oil and gas accumulations* (Vol. 5): Editions TECHNIP.

Persson, P.-O., & Strang, G. (2004). A simple mesh generator in MATLAB. *SIAM review, 46*(2), 329-345.

Raleigh, C., Healy, J., & Bredehoeft, J. (1976). An experiment in earthquake control at Rangely, Colorado. *Science, 191*(4233), 1230-1237.

Rietveld, H. (1986). *Land subsidence in the Netherlands.* Paper presented at the Proceedings of the 3rd international symposium on land subsidence.

Rondeel, H., Batjes, D., & Nieuwenhuijs, W. (1996). *Geology of Gas and Oil under the Netherlands*: Springer Science & Business Media.

Røste, T., Stovas, A., & Landrø, M. (2006). Estimation of layer thickness and velocity changes using 4D prestack seismic data. *Geophysics, 71*(6), S219-S234.

Segall, P. (1989). Earthquakes triggered by fluid extraction. *Geology, 17*(10), 942-946.

Segall, P. (1992). Induced stresses due to fluid extraction from axisymmetric reservoirs. *Pure and Applied Geophysics, 139*(3-4), 535-560.

Segall, P., Grasso, J. R., & Mossop, A. (1994). Poroelastic stressing and induced seismicity near the Lacq gas field, southwestern France. *Journal of Geophysical Research: Solid Earth (1978–2012), 99*(B8), 15423-15438.

Segura, J., Fisher, Q., Crook, A., Dutko, M., Yu, J., Skachkov, S., . . . Kendall, J. (2011). Reservoir stress path characterization and its implications for fluid-flow production simulations. *Petroleum Geoscience, 17*(4), 335-344.

Shearer, P. M. (2009). *Introduction to seismology*: Cambridge University Press.

Sornette, A., & Sornette, D. (1989). Self-organized criticality and earthquakes. *EPL (Europhysics Letters), 9*(3), 197.

Stauble, A., & Milius, G. (1970). Geology of Groningen gas field, Netherlands.

Suckale, J. (2009). Induced seismicity in hydrocarbon fields. *Advances in geophysics, 51*, 55-106.

Teufel, L. W., Rhett, D. W., & Farrell, H. E. (1991). *Effect of reservoir depletion and pore pressure drawdown on in situ stress and deformation in the Ekofisk field, North Sea.* Paper presented at the The 32nd US Symposium on Rock Mechanics (USRMS).

Turcotte, D. L. (1999). Self-organized criticality. *Reports on progress in physics, 62*(10), 1377.

Van Balen, R., Houtgast, R., & Cloetingh, S. (2005). Neotectonics of The Netherlands: a review. *Quaternary Science Reviews, 24*(3), 439-454.

Van Eck, T., Goutbeek, F., Haak, H., & Dost, B. (2006). Seismic hazard due to small-magnitude, shallow-source, induced earthquakes in The Netherlands. *Engineering Geology, 87*(1), 105-121.

Van Eijs, R. M. H. E., Mulders, F. M. M., Nepveu, M., Kenter, C. J., & Scheffers, B. C. (2006). Correlation between hydrocarbon reservoir properties and induced seismicity in the Netherlands. *Engineering Geology, 84*(3–4), 99-111. doi: http://dx.doi.org/10.1016/j.enggeo.2006.01.002

van Elk, J., & Doornhof, D. (2012). Study and Data Acquisition Plan for Induced Seismicity in Groningen.

van Thienen-Visser, K., & Breunese, J. (2015). Induced seismicity of the Groningen gas field: History and recent developments. *The Leading Edge, 34*(6), 664-671.

Van Wees, J., Buijze, L., Van Thienen-Visser, K., Nepveu, M., Wassing, B., Orlic, B., & Fokker, P. (2014). Geomechanics response and induced seismicity during gas field depletion in the Netherlands. *Geothermics, 52*, 206-219.

Warpinski, N. R. (2013). *Understanding Hydraulic Fracture Growth, Effectiveness, and Safety Through Microseismic Monitoring.* Paper presented at the ISRM International Conference for Effective and Sustainable Hydraulic Fracturing.

Zoback, M. D., & Gorelick, S. M. (2012). Earthquake triggering and large-scale geologic storage of carbon dioxide. *Proceedings of the National Academy of Sciences, 109*(26), 10164-10168.

Zoback, M. D., & Zinke, J. C. (2002). Production-induced normal faulting in the Valhall and Ekofisk oil fields *The Mechanism of Induced Seismicity* (pp. 403-420): Springer.

Appendix A: Mesh generator in MatLab

```
%Meshgenerator kompatibel med MDEM
clear all;
addpath('distmesh')
fstats=@(p,t) fprintf('%d nodes, %d elements, min quality %.2f\n',
...
                      size(p,1),size(t,1),min(simpqual(p,t)));

a = 5000; b = 3000; c = 2000; d = 120;
h = 25;
% a, b, c og d definerer "boksene" i modellen
% h er kantlinjen i startdistribusjonen. Desto mindre h, desto
finere mesh.

fd = @(p) drectangle(p,-a,a,-b,b);
% fd beskriver domenet til meshet.

m = 200;
fh = @(p) max(drectangle(p,-c,c,-d,d)+m,m);
%{
% fh funksjonen skal beskrive hvor stor kantlinjen til et element er
i
% forhold til de andre elementene, ut fra hvor elementene befinner
seg i
% domenet.
% Her har jeg sagt at den relative kantlinjen skal v?re lik det
tallet som
% er st?rst av "m" og "drectangle(p,-c,c,-d,d)+m". Det vil si at
kantlinjen
% alltid er lik innenfor den lille boksen (for her er "m" st?rst)
mens den
% blir gradvis st?rre fra den lille boksen til den store.
%}
box = [-a -b; a b];

fixed = [-a b; -a -b; a -b; a b];
%{
% [p, t] er funksjonen som faktisk lager meshet. Den lagrer punktene
til
% alle hj?rner i matrisen p, og indeksen til alle hj?rnene i
trekantene i
% matrisen t.
%}
[p, t] = distmesh2d(fd, fh, h, box, fixed);

edge = freeBoundary(triangulation(t,p));
save('edge.mat', 'edge')
save('p.mat', 'p')
save('t.mat', 't')
%%%%%%%%%%%%%%%%%%%%%%%%%%%%%%%%%%%%%%%%%%%%%%%%%%%%%%%
%load('edge'); load('p'); load('t');
%{
%fstats(p,t);
%VX=p(:,1);
%VY=p(:,2);
%}
```

```
%Toppnoder
count = 1;
for i=1:length(edge(:,1))
    if abs((p(edge(i,1),2) + p(edge(i,2),2))/2 - b) < 0.1
        top(count,:) = edge(i,:);
        count = count + 1;
    end
end

%Bunnoder
count = 1;
for i=1:length(edge(:,1))
    if abs((p(edge(i,1),2) + p(edge(i,2),2))/2 + b) < 0.1
        bottom(count,:) = edge(i,:);
        count = count + 1;
    end
end

%H?yrenoder
count = 1;
for i=1:length(edge(:,1))
    if abs((p(edge(i,1),1) + p(edge(i,2),1))/2 - a) < 0.1
        right(count,:) = edge(i,:);
        count = count + 1;
    end
end

%Venstrenoder
count = 1;
for i=1:length(edge(:,1))
    if abs((p(edge(i,1),1) + p(edge(i,2),1))/2 + a) < 0.1
        left(count,:) = edge(i,:);
        count = count + 1;
    end
end
%Manipulating matrices for fprintf
P=[[1:size(p,1)]',p(:,1),p(:,2)]';
T=[[1:size(t,1)]',t(:,1),t(:,2),t(:,3)]';

%Elements
Elements=T';
Nodes=P';

P=P';
T=T';
%Toppelement
count=1;
unitop=unique(top);
for i=1:length(Elements)
    for k=2:4
        for teller=1:length(unitop)
            if Elements(i,k)==unitop(teller)==1
                Eltop(count,:)=Elements(i,1);
                count=count+1;
            end
        end
    end
```

```
end
Eltop=unique(Eltop);

%Bunnelement
count=1;
unibottom=unique(bottom);
for i=1:length(Elements)
    for k=2:4
        for teller=1:length(unibottom)
            if Elements(i,k)==unibottom(teller)==1
                Elbottom(count,:)=Elements(i,1);
                count=count+1;
            end
        end
    end
end
Elbottom=unique(Elbottom);

%H?yreelement
count=1;
uniright=unique(right);
for i=1:length(Elements)
    for k=2:4
        for teller=1:length(uniright)
            if Elements(i,k)==uniright(teller)==1
                Elright(count,:)=Elements(i,1);
                count=count+1;
            end
        end
    end
end
Elright=unique(Elright);

%Vensteelement
count=1;
unileft=unique(left);
for i=1:length(Elements)
    for k=2:4
        for teller=1:length(unileft)
            if Elements(i,k)==unileft(teller)==1
                Elleft(count,:)=Elements(i,1);
                count=count+1;
            end
        end
    end
end
Elleft=unique(Elleft);

%Reservoirnoder1
count=1;
for i=1:length(Nodes)
    if abs(Nodes(i,2))<=c/2 && abs(Nodes(i,3))<=d
        intres1(count)=Nodes(i,1);
        count=count+1;
    end
end
%{
```

```
Reservoirnoder2
count=1;
for i=1:length(Nodes)
    if abs(Nodes(i,2))<=c && abs(Nodes(i,2))>c/2 &&
abs(Nodes(i,3))<=d
        intres2(count)=Nodes(i,1);
        count=count+1;
    end
end
%}
%Overburdennoder
count=1;
for i=1:length(Nodes)
    if abs(Nodes(i,2))>c && abs(Nodes(i,3))>d
        exres(count)=Nodes(i,1);
        count=count+1;
    end
end
%{
%Liste indre elementer
indreElementer=setdiff(Elements,Eltop);
indreElementer=setdiff(indreElementer,Elbottom);
indreElementer=setdiff(indreElementer,Elleft);
indreElementer=setdiff(indreElementer,Elright);

%alle indre elemeter m/noder= interiorElements
count=1;
for i=1:length(Elements)
    for k=1:length(indreElementer)
        if Elements(i,1)==indreElementer(k)==1
            interiorElements(count,:)=Elements(i,:);
            count=count+1;
        end
    end
end
%}
% Deklarer tellere for vektorene lille og store
lilleTeller = 1; storeTeller = 1; mellomTeller = 1; FTeller = 1;
%G?r igjennom alle noder i indre elementer
for i=1:length(Elements)

        % Hvis punktene er innenfor Faults, Res eller OB legges
detil
        if abs(-p(Elements(i,2),1)-p(Elements(i,2),2)/2+c/2) <=1.1*h
&& abs(p(Elements(i,2),2)) <= 2*d && abs(-p(Elements(i,3),1)-
p(Elements(i,3),2)/2 + c/2) <= 1.1*h && abs(p(Elements(i,3),2)) <=
2*d && abs(-p(Elements(i,4),1) - p(Elements(i,4),2)/2+c/2) <= 1.1*h
&& abs(p(Elements(i,4),2)) <= 2*d
        FElements(FTeller) = Elements(i,1);
        FTeller = FTeller + 1;
        elseif abs(p(Elements(i,2),1)-p(Elements(i,2),2)/2+c/2) <=
1.1*h && abs(p(Elements(i,2),2)) <= 2*d && abs(+p(Elements(i,3),1)-
p(Elements(i,3),2)/2 + c/2) <= 1.1*h && abs(p(Elements(i,3),2)) <=
2*d && abs(+p(Elements(i,4),1) - p(Elements(i,4),2)/2 + c/2) <=
1.1*h && abs(p(Elements(i,4),2)) <= 2*d
        FElements(FTeller) = Elements(i,1);
        FTeller = FTeller + 1;
```

```
    elseif abs(-p(Elements(i,2),1)-p(Elements(i,2),2)/2+c)
<=1.1*h && abs(p(Elements(i,2),2)) <= 4*d && abs(-
p(Elements(i,3),1)-p(Elements(i,3),2)/2 + c) <= 1.1*h &&
abs(p(Elements(i,3),2)) <= 4*d && abs(-p(Elements(i,4),1) -
p(Elements(i,4),2)/2+c) <= 1.1*h && abs(p(Elements(i,4),2)) <= 4*d
    FElements(FTeller) = Elements(i,1);
    FTeller = FTeller + 1;
    elseif abs(p(Elements(i,2),1)-p(Elements(i,2),2)/2+c)
<=1.1*h && abs(p(Elements(i,2),2)) <= 4*d && abs(p(Elements(i,3),1)-
p(Elements(i,3),2)/2 + c) <= 1.1*h && abs(p(Elements(i,3),2)) <= 4*d
&& abs(p(Elements(i,4),1) - p(Elements(i,4),2)/2+c) <= 1.1*h &&
abs(p(Elements(i,4),2)) <= 4*d
    FElements(FTeller) = Elements(i,1);
    FTeller = FTeller + 1;
    %Res1
    elseif (p(Elements(i,2),1)+p(Elements(i,2),2)/2 <= c/2 && -
p(Elements(i,2),1)+p(Elements(i,2),2)/2 <= c/2 &&
abs(p(Elements(i,2),2)) <= 1.2*d &&
p(Elements(i,3),1)+p(Elements(i,3),2)/2 <= c/2 && -
p(Elements(i,3),1)+p(Elements(i,3),2)/2 <= c/2 &&
abs(p(Elements(i,3),2)) <= 1.2*d && p(Elements(i,4),1) +
p(Elements(i,4),2)/2 <= c/2 && -p(Elements(i,4),1) +
p(Elements(i,4),2)/2 <= c/2 && abs(p(Elements(i,4),2)) <= 1.2*d)
    ResElements1(lilleTeller) = Elements(i,1);
    lilleTeller = lilleTeller + 1;
    %Res2
    elseif (p(Elements(i,2),1)+p(Elements(i,2),2)/2 <= c && -
p(Elements(i,2),1)+p(Elements(i,2),2)/2 <= c &&
abs(p(Elements(i,2),2)) <= d &&
p(Elements(i,3),1)+p(Elements(i,3),2)/2 <= c && -
p(Elements(i,3),1)+p(Elements(i,3),2)/2 <= c &&
abs(p(Elements(i,3),2)) <= d &&
p(Elements(i,4),1)+p(Elements(i,4),2)/2 <= c && -
p(Elements(i,4),1)+p(Elements(i,4),2)/2 <= c &&
abs(p(Elements(i,4),2)) <= d)
    ResElements2(mellomTeller) = Elements(i,1);
    mellomTeller = mellomTeller + 1;
    % Hvis ikke, legg dem til Ob
    else
    ObElements(storeTeller) = Elements(i,1);
    storeTeller = storeTeller +1;
    end
end
fid=fopen('Example_mesh.inp', 'w');
fprintf(fid, '**Try\r\n** Job name: resmesh Model name: reserv\r\n**
Generated by: OP *Preprint, echo=NO, model=NO, history=NO,
contact=NO\r\n**\r\n**PARTS\r\n**\r\n*Part, name=RockPart\r\n');
fprintf(fid, '*Node\r\n');
for q=1:length(P)
  P(q,2)=P(q,2)+a;
  P(q,3)=P(q,3)+b;
end
for i=1:length(P)
  for k=1:3
    if (mod(k,3)==0)
      fprintf(fid, '\t%d\n',P(i,k));
    else
```

```
            fprintf(fid, '\t%d,',P(i,k));
        end
    end
end

fprintf(fid, '*Element, type=CPS3\r\n');
for i=1:length(T)
    for k=1:4
        if (mod(k,4)==0)
            fprintf(fid, '\t%d\n',T(i,k));
        else
            fprintf(fid, '\t%d,',T(i,k));
        end
    end
end
%fprintf(fid, '\t%d, \t%d, \t%d, \t%d\r\n', T);
fprintf(fid, '*Nset, nset=TopSide\r\n');
fprintf(fid, '\t%d',top(1,1));
for i=1:length(top)
    if(mod(i,16)==0)
        fprintf(fid, '\n\t%d',top(i,2)');
    else
        fprintf(fid, ',\t%d',top(i,2));
    end
end
fprintf(fid, '\r\n*Elset, elset=TopSide\r\n');
for i=1:length(Eltop)
    if(mod(i,16)==0)
        fprintf(fid, '\t%d\n',Eltop(i)');
    elseif i==length(Eltop)
        fprintf(fid, '\t%d\n',Eltop(i)');
    else
        fprintf(fid, '\t%d,',Eltop(i));
    end
end
fprintf(fid, '*Nset, nset=BottomSide\r\n');
fprintf(fid, '\t%d',bottom(1,1));
for i=1:length(bottom)
    if(mod(i,16)==0)
        fprintf(fid, '\n\t%d',bottom(i,2)');
    else
        fprintf(fid, ',\t%d',bottom(i,2));
    end
end
fprintf(fid, '\r\n*Elset, elset=BottomSide\r\n');
for i=1:length(Elbottom)
    if(mod(i,16)==0)
        fprintf(fid, '\t%d\n',Elbottom(i)');
    elseif i==length(Elbottom)
        fprintf(fid, '\t%d\n',Elbottom(i)');
    else
        fprintf(fid, '\t%d,',Elbottom(i));
    end
end
fprintf(fid, '*Nset, nset=LeftSide\r\n');
fprintf(fid, '\t%d',left(1,1));
for i=1:length(left)
```

```
    if(mod(i,16)==0)
        fprintf(fid, '\n\t%d',left(i,2)');
    else
        fprintf(fid, ',\t%d',left(i,2));
    end
end
fprintf(fid, '\r\n*Elset, elset=LeftSide\r\n');
for i=1:length(Elleft)
    if(mod(i,16)==0)
        fprintf(fid, '\t%d\n',Elleft(i)');
    elseif i==length(Elleft)
        fprintf(fid, '\t%d\n',Elleft(i)');
    else
        fprintf(fid, '\t%d,',Elleft(i));
    end
end
fprintf(fid, '*Nset, nset=RightSide\r\n');
fprintf(fid, '\t%d',right(1,1));
for i=1:length(right)
    if(mod(i,16)==0)
        fprintf(fid, '\n\t%d',right(i,2)');
    else
        fprintf(fid, ',\t%d',right(i,2));
    end
end
fprintf(fid, '\r\n*Elset, elset=RightSide\r\n');
for i=1:length(Elright)
    if(mod(i,16)==0)
        fprintf(fid, '\t%d\n',Elright(i)');
    elseif i==length(Elright)
        fprintf(fid, '\t%d\n',Elright(i)');
    else
        fprintf(fid, '\t%d,',Elright(i));
    end
end
fprintf(fid, '*Elset, elset=Faults\r\n');
for i=1:length(FElements)
    if(mod(i,16)==0)
        fprintf(fid, '\t%d\n',FElements(i)');
   elseif i==length(FElements)
        fprintf(fid, '\t%d\n',FElements(i)');
    else
        fprintf(fid, '\t%d,',FElements(i));
    end
end
fprintf(fid, '*Elset, elset=Reservoir1\r\n');
for i=1:length(ResElements1)
    if(mod(i,16)==0)
        fprintf(fid, '\t%d\n',ResElements1(i)');
   elseif i==length(ResElements1)
        fprintf(fid, '\t%d\n',ResElements1(i)');
    else
        fprintf(fid, '\t%d,',ResElements1(i));
    end
end
fprintf(fid, '*Elset, elset=Reservoir2\r\n');
for i=1:length(ResElements2)
```

```
    if(mod(i,16)==0)
        fprintf(fid, '\t%d\n',ResElements2(i)');
   elseif i==length(ResElements2)
        fprintf(fid, '\t%d\n',ResElements2(i)');
    else
        fprintf(fid, '\t%d,',ResElements2(i));
    end
end
fprintf(fid, '*Elset, elset=Overburden\r\n');
for i=1:length(ObElements)
    if(mod(i,16)==0)
        fprintf(fid, '\t%d\n',ObElements(i)');
    elseif i==length(ObElements)
        fprintf(fid, '\t%d\n',ObElements(i)');
    else
        fprintf(fid, '\t%d,',ObElements(i));
    end
end
fprintf(fid, '*Elset, elset=ReservoirZone1\n')
for i=1:length(ResElements1)
    if(mod(i,16)==0)
        fprintf(fid, '\t%d\n',ResElements1(i)');
   elseif i==length(ResElements1)
        fprintf(fid, '\t%d\n',ResElements1(i)');
    else
        fprintf(fid, '\t%d,',ResElements1(i));
    end
end
fprintf(fid, '*Elset, elset=ReservoirZone2\n')
for i=1:length(ResElements2)
    if(mod(i,16)==0)
        fprintf(fid, '\t%d\n',ResElements2(i)');
   elseif i==length(ResElements2)
        fprintf(fid, '\t%d\n',ResElements2(i)');
    else
        fprintf(fid, '\t%d,',ResElements2(i));
    end
end
fprintf(fid, '*Elset, elset=OverburdenZone\n')
for i=1:length(ObElements)
    if(mod(i,16)==0)
        fprintf(fid, '\t%d\n',ObElements(i)');
    elseif i==length(ObElements)
        fprintf(fid, '\t%d\n',ObElements(i)');
    else
        fprintf(fid, '\t%d,',ObElements(i));
    end
end
fprintf(fid, '*Elset, elset=FZone\n')
for i=1:length(FElements)
    if(mod(i,16)==0)
        fprintf(fid, '\t%d\n',FElements(i)');
   elseif i==length(FElements)
        fprintf(fid, '\t%d\n',FElements(i)');
    else
        fprintf(fid, '\t%d,',FElements(i));
    end
```

```
end
fprintf(fid, '** Section: ReservoirSection1\n*Solid Section,
elset=ReservoirZone1, material=Reservoir1 \n,\n');
fprintf(fid, '** Section: ReservoirSection2\n*Solid Section,
elset=ReservoirZone2, material=Reservoir2 \n,\n');
fprintf(fid, '** Section: OverburdenSection\n*Solid Section,
elset=OverburdenZone, material=OB \n,\n');
fprintf(fid, '** Section: FaultSection\n*Solid Section, elset=FZone,
material=Fault \n,\n');
fprintf(fid, '*End Part\n*End Instance\n **\n');
fprintf(fid, '*End Assembly\n **');
fclose(fid);
```